Automotive Waste Heat Recovery:

A Semi-Truck Exhaust Application

A Major Qualifying Project
Submitted to the Faculty of

WORCESTER POLYTECHNIC INSTITUTE

in partial fulfillment for the
Bachelor of Science Degree
In Mechanical Engineering

Submitted By:
Max Frohlich, ME
Alana Guilbault, ME
Kevin Mercier, ME
Evan Ryan, ME

Advised By:
Professor Fiona Levey, ME

Date of Submission:
May 3, 2021

Table of Contents

List of Figures

List of Tables

Abbreviations

A - Area [m^2]

Bi_2Te_3- Bismuth telluride

c_p- Specific heat [$J/kg \cdot K$]

D_i- Inner diameter [m]

D_o- Outer diameter [m]

E - Young's Modulus [Pa]

ε - Strain

f - Friction factor

F_c - Compressive force [N]

F_g - Force of gravity [N]

F_y - Force in y-direction [N]

h_i- Inner Convective Heat Transfer Coefficient [$W/m^2 \cdot K$]

h_o- Outer Convective Heat Transfer Coefficient [$W/m^2 \cdot K$]

k - Thermal conductivity [$W/m \cdot K$]

L - Length [m]

m - Mass [kg]

ṁ - Mass flow rate [kg/s]

Nu_D- Nusselt Number

η_{ALT} - Alternator efficiency

η_{EG} - Exhaust gases efficiency

η_{ENG} - Engine efficiency

η_{TEG} - Thermoelectric generator efficiency

η_{th}- Thermal efficiency

σ - Stress [Pa]

ρ- Density [kg/m^3]

P_o - Power [W]

Pr - Prandtl Number

PEO - Plasma electrolytic oxidation

Re_D- Reynolds Number

R_{tot}- Total resistivity [K/W]

t - Wall thickness [m, in]

T_{Ave}- Average temperature [K, ℃]

T_∞- Ambient temperature [K, ℃]

$T_{m,i}$- Temperature in [K, ℃]

$T_{m,o}$- Temperature out [K, ℃]

TEG(s) - Thermoelectric generator(s)

μ- Dynamic viscosity [$kg/m \cdot s$]

V - Velocity [m/s, MPH]

Abstract

The goal of this project was to determine the feasibility of using thermoelectric generation as a method of collecting waste heat from a standard semi-truck exhaust system. Prior research regarding the efficacy of thermoelectric generators to reclaim wasted energy in mechanical processes inspired this project. A device for housing thermoelectric generators on the exhaust stack of a semi-truck was designed and optimized based on its structural integrity, potential power generation, and subsequent cost savings. Results from simulation models predict that the device would improve fuel efficiency by at least 4.96%.

Acknowledgements

We would like to give special thanks to those that furthered our education and research skills. Great thanks to our advisor, Professor Fiona Levey, for her support and guidance to complete this Major Qualifying Project.

We would also like to thank Dr. Adriana Hera for her instruction and assistance in further developing our technical skills and knowledge as engineers.

Lasty, we would like to thank our friends, families, and classmates for their continuous encouragement throughout all our endeavors as students.

1.0 Introduction

Modern dependence on petroleum-based fuels has contributed significantly to global warming and a rise in greenhouse gases. In 2018, transportation alone accounted for 28% of the United States' greenhouse gas emissions, with heavy-duty trucks accounting for 23% of these emissions (EPA, 2018). The typical commercial truck in the United States will emit 161.8 grams of CO_2 per ton mile (Mathers, 2014). Trucking is a $791.7 billion industry that accounts for 5% of all full-time jobs in the United States, so it is unlikely to expect a sizable decrease in the coming years to mitigate carbon emissions.

The need to decrease greenhouse gas emissions has driven research into improving engine efficiencies and utilizing waste heat. Thermoelectric technology is considered an evolving solution to convert waste heat into electrical energy. A part of this emerging technology is thermoelectric generators (TEGs), which use a temperature difference between two ceramic plates with semiconductors sandwiched in between to create a DC power source. The process of generating power from a temperature difference is a phenomenon known as the Seebeck effect. The goal of this project was to investigate the power generating potential from waste heat produced by a semi-trailer truck using an array of thermoelectric generator modules primarily through simulations. We have proposed a design for a TEG housing module that would be attached externally to the vertical exhaust stack of a semi-truck using the exhaust gases as a heat source and forced air convection from driving as the cooling method.

2.0 Background

2.1 Thermoelectric Generators

Thermoelectric generators are devices that utilize the Seebeck and Peltier effects to convert thermal energy into electrical energy and vice versa (Jaziri et al., 2019). These devices are a promising step forward towards harvesting cleaner and more renewable energy because they do not contain chemical products and do not require moving mechanical components. TEGs can be used in several applications, such as recovering waste heat, supplying low powered systems, and creating thermal energy in extreme situations (Dufo-López et al., 2019). Figure 1 shows a TEG configuration where there are three main components to the module: a hot plate, a cold plate, and p&n-type semiconductors in between the plates.

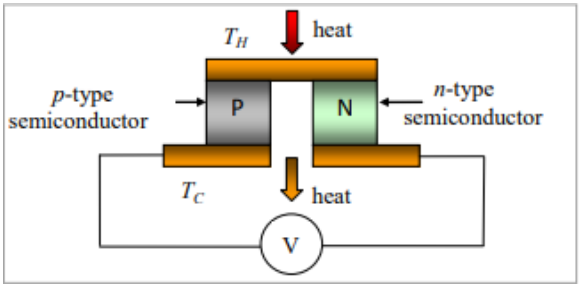

Figure 1. Thermoelectric Module Schematic

These thermoelectric generating modules are connected electrically in series, but thermally in parallel in order to maximize their efficiencies. When there is a temperature difference between the hot and cold side plates, a voltage is produced. The amount of produced voltage depends on the magnitude of the gradient, and the Seebeck coefficient (Mamur, 2019).

In regards to the efficiencies of TEGs, there is an important dimensionless variable known as the figure of merit. When the figure of merit is increased, the efficiency, and therefore, the power output also increases (Chen et al., 2016). The most common semiconductor material for thermoelectric generators is Bismuth Telluride (Bi_2Te_3), because it has the highest thermoelectric figure of merit at room temperature, thus producing optimal efficiencies. (Witting et al., 2019).

The efficiencies of present-day TEGs are low. Modern TEGs have efficiencies from 5% to 15%, and, in waste heat recovery systems, only reach up to around 6%. (Enescu, 2018). All of the waste heat that is not captured by TEGs is lost.

The power output of TEGs are also low, relative to other systems of power generation. In general, one TEG can produce between 1 Watt and 125 Watts of power (Enescu, 2018). This is not a large amount of power, but putting multiple TEGs into a system can increase the total power output.

2.2 Internal Combustion Engines

In gasoline fueled internal combustion engines, only 30% of the fuel combustion energy is converted to mechanical energy. Efficiencies are equal to the work of the engine divided by the thermal energy from the fuel (Suppes & Storvick, 2016). The remaining energy is lost through waste heat: 40% through the exhaust gas and 30% through the engine coolant (Kim et al., 2011). In comparison to gasoline engines, diesel engines are about 10% more efficient. The efficiency of an average 4-stroke diesel engine is about 40% (Suppes & Storvick, 2016). The exhaust gases emitted into the atmosphere from internal combustion engines are large contributors to greenhouse gas emissions in transportation. The need to decrease carbon emissions has driven research for improving engine efficiencies, particularly in utilizing the significant amount of waste heat generated. Exhaust gases from these engines are capable of reaching high temperatures, typically discharging at approximately 420℃ (Nolan, 2017). This coupled with the exhaust system's ease of accessibility makes the exhaust pipe an ideal setting for heat collection.

Thermoelectric generators (TEGs) were first implemented inside automobiles in 1963. In the latter half of the 20th century, early prototypes were developed by Porsche, Hi-Z Technology, Nissan Motors, and General Motors in collaboration with Clarkson University (Saqr & Musa, 2009). Nissan tested a 3-liter gasoline engine using silicon-germanium modules, producing a maximum thermoelectric conversion efficiency of 2%. General Motors tested an 8-liter gasoline engine and produced an efficiency of 2.9% using bismuth telluride thermoelectric modules. Hi-Z Technology tested a Cummins 14-liter diesel engine and achieved an efficiency of 4.5% (Saqr & Musa, 2009) with bismuth telluride modules (Weng & Huang, 2013). Each of

these TEGs used exhaust gases as their hot temperature and engine coolant as their cold temperature (Saqr & Musa, 2009).

2.3 TEG Selection

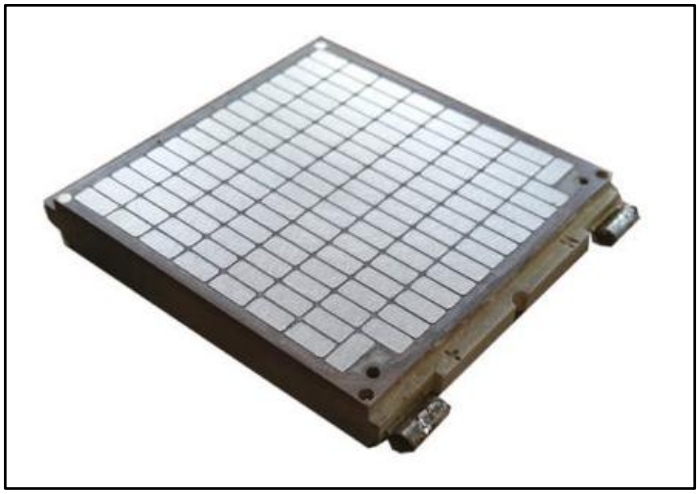

Figure 2. Hi-Z 14HV Thermoelectric Module

When comparing available thermoelectric generators on the market, we considered the expected power output, temperature limitations, efficiency, cost, and life expectancy of each module. We compared a variety of TEGs from different companies such as Ferrotec, TEGmart, and Hi-Z Technology. For our device, the HZ-14HV module offered by Hi-Z Technology, as shown in Figure 2, was determined to be the best fit for our design and simulation requirements. Our final design includes 24 of these 61.05 millimeters by 71.05 millimeters bismuth telluride modules, each weighing 65 grams. In comparison to other thermoelectric generators the HZ-14HV produced the highest power and had the greatest efficiency, at a price of $25 per module. Hi-Z Technology also claims that if used properly and does not exceed a temperature of 250℃, these modules would last greater than ten years, however, these modules can operate intermittently beyond 350℃ (Hi-Z Technology, 2020).

Figures 3 and 4 are the power and efficiency results of the HZ-14HV module provided by Hi-Z Technology that were used in Section 7.3 (Hi-Z Technology, 2020).

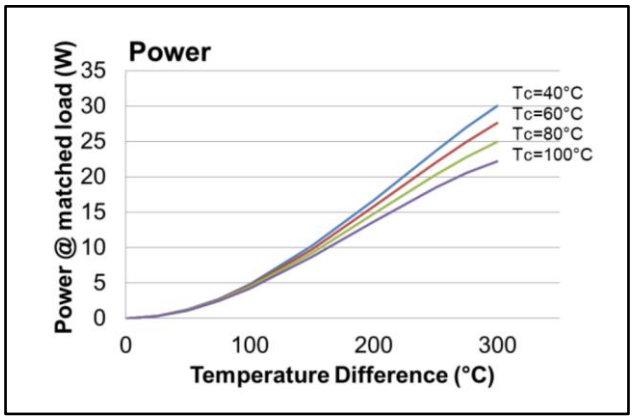

Figure 3. Graph of Thermoelectric Generator Power (Hi-Z Technology, 2020)

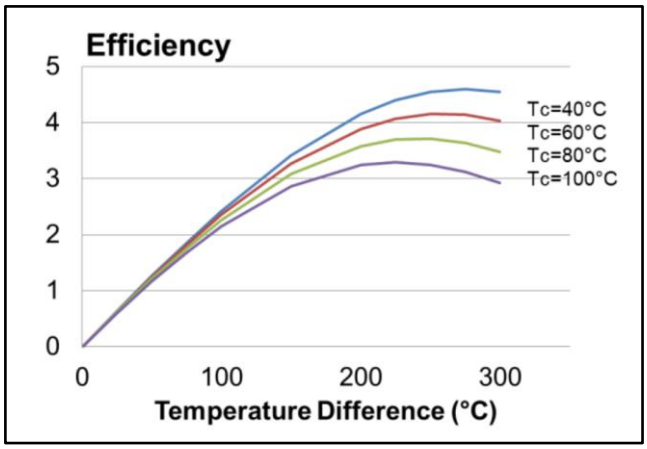

Figure 4. Graph of Thermoelectric Generator Efficiency (Hi-Z Technology, 2020)

3.0 Preliminary Design

For this MQP, various options concerning energy generating systems were considered. From the start, the goal was to reclaim waste heat to improve the efficiency of a machine process. Using waste heat as an energy source has the potential to save companies a large amount of money and energy in the long run. The initial plan for this project was to implement thermoelectric generators into a wind turbine, specifically in the turbine's generator where it would harvest the waste heat. A lack of temperature experimentations and specific dimensions on wind turbine generator systems led the team to conclude that an alternative system would be better suited for the application of thermoelectric generators.

A modern thermoelectric generator study published in 2016 used a turbocharged, six-cylinder diesel engine, the type usually seen in a semi-truck. This study utilized the temperature difference through the exhaust pipe and engine coolant. The thermoelectric modules generated a maximum energy conversion efficiency of about 2.8% (Kim et al., 2016). This study inspired our project to harness the waste heat from the exhaust stack of a semi-truck and to use wind from normal vehicle operation as the cooling fluid.

We determined that diesel engines are a better application for TEGs rather than regular gas engines. Diesel engines experience moderate to high engine loads for a long period of time, whereas regular gas driven cars are usually being driven for short periods of time comparatively. This means the thermoelectric assembly can harvest a larger amount of waste heat in a commercially driven diesel truck. Additionally, gas powered cars do not have exhaust stacks, so the assembled device would need to be fitted somewhere else similar to the tailgate exhaust pipe system. Our thinking was that forced convection in the form of wind from normal vehicle operation would be the most cost effective method as the TEG cold side fluid, so exposed vertical exhaust stacks in semi-trucks would be more practical than exhaust pipes in gas engine vehicles. We saw more opportunity here to implement TEGs into a semi-truck exhaust system that could potentially have a massive commercial appeal rather than for consumers wanting TEGs installed in their gas vehicles.

In the first iteration of our design, the TEGs attached directly to the surface of the exhaust pipe. However, this proved impractical due to the curvature of the pipe creating an uneven surface to apply adhesive, as well as creating a variety of hot spots on the pipe. Diesel engine exhaust gas normally discharges from the exhaust stack at a temperature of about 420°C (Nolan, 2017), which means the surface of the exhaust stack itself would be too hot to directly put the TEGs on. Our solution to this problem was creating a hexagonal wall that the TEGs would be attached to and still experience heat transfer. The wall is in a hexagon shape so that the unbendable TEGs may be attached to straight, flat surfaces. This hexagonal wall was mainly used to reduce the thermal conduction of the heat radiating from the exhaust pipe itself because of the high exhaust gas temperatures and the service limitations of our Hi-Z 14HV thermoelectric modules. The TEGs can only operate continuously at 250°C and intermittently beyond 350°C (Hi-Z Technology, 2020). To prevent our TEGs from overheating, and deteriorating from hot exhaust gas temperatures, we considered designing the hexagonal wall using a material with low thermal conductivity. However, we also considered materials with high thermal conductivity because of their overall lower costs and structural properties. Simulation results, later to be discussed, determined the viability of the materials considered.

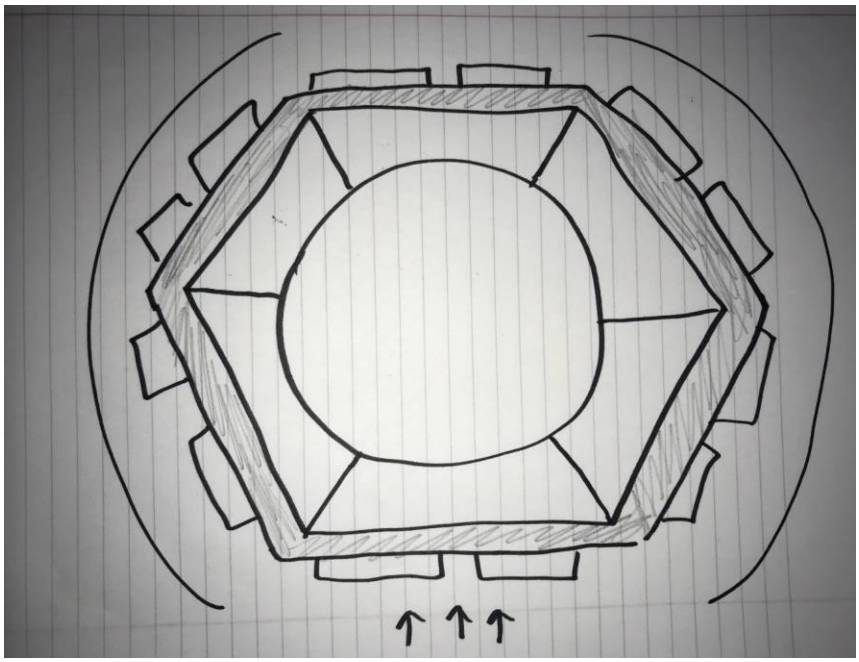

Figure 5. Hand Drawn Sketch of Top View of Preliminary Design

Figure 5 shows a hand drawing of our initial design. The arrows at the bottom of the image indicate the direction of air flow from normal vehicle operation. We wanted to optimize the number of TEGs we had on our device, so there were two TEGs per side on the hexagonal wall. To protect the electronic components of the exposed TEGs from weather, we thought about designing a protective outer shield surrounding the entire device. The protective shield had one opening and one closing to have a simple flow of air around the TEGs. However, structurally, we considered designing a slotted shield that wrapped around the entire device and exhaust pipe as shown in Figure 6. This allowed for more airflow for the cold side of the TEGs as well as protection from harsh weather conditions.

Figures 6-9 are SOLIDWORKS drawings of our first thermoelectric generator assembly design around an exhaust stack. For commercial semi-trucks, an exhaust stack with an 6-inch inner diameter is very common, so we based our device around this dimension (TruckPipesUSA.com, 2020). We changed the number of TEGs per row on the hexagonal wall side from two to one. In this preliminary design, the whole length of the device was 0.5 meters and there were six supporting wall structures. This would mean that the device would house 30 TEGs, with each face of the hexagonal wall having five rows of modules equally spaced apart.

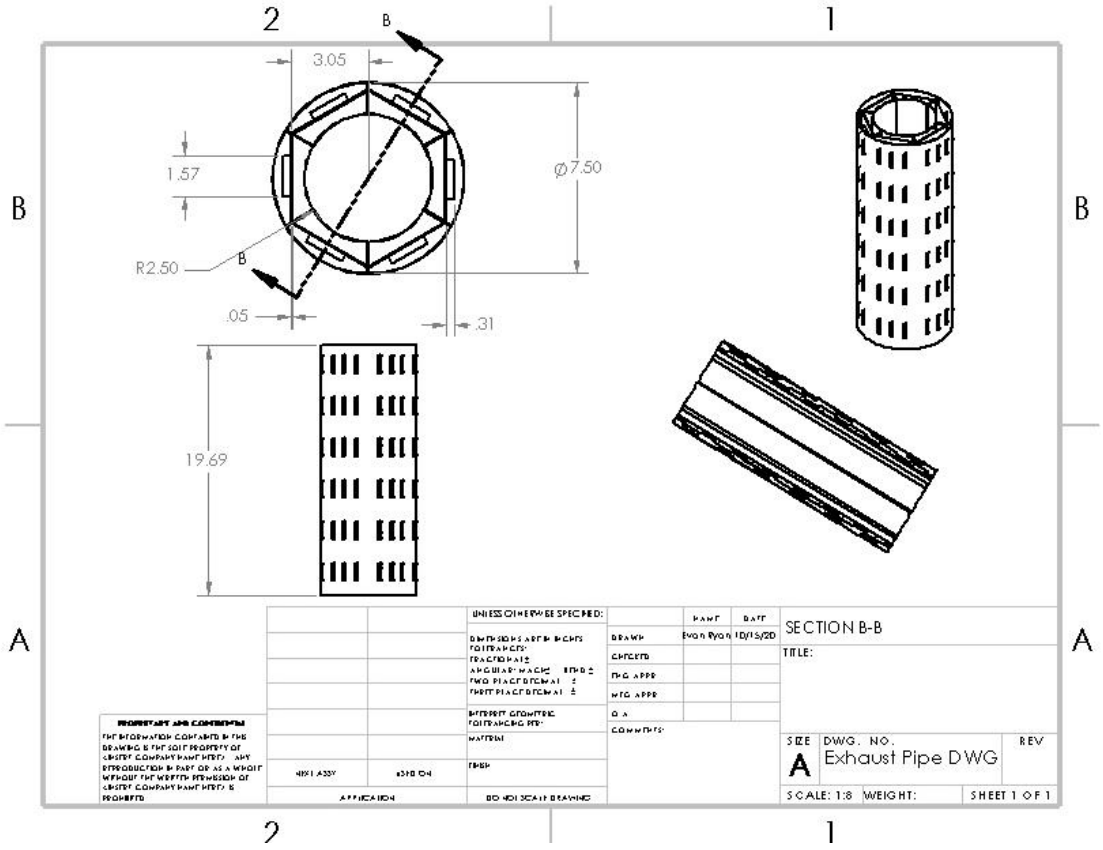

Figure 6. SOLIDWORKS Drawing of First Design Iteration

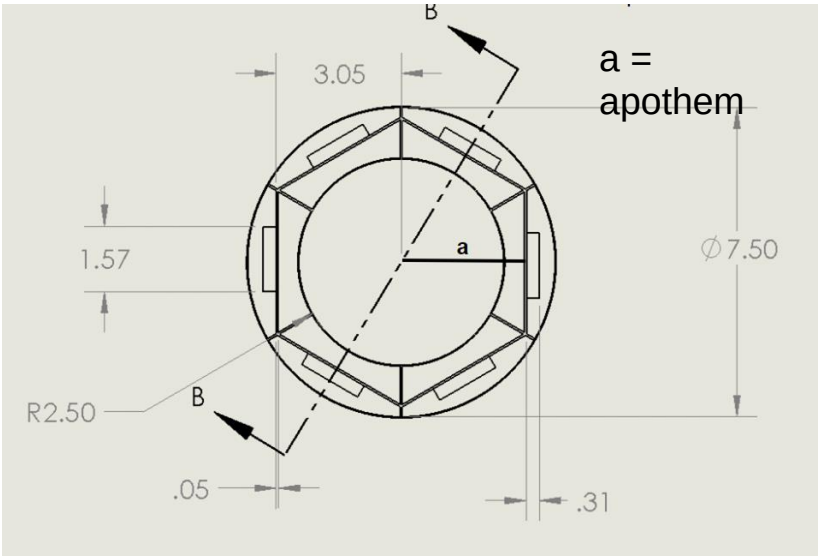

Figure 7. Top View of First Design Iteration (Inches)

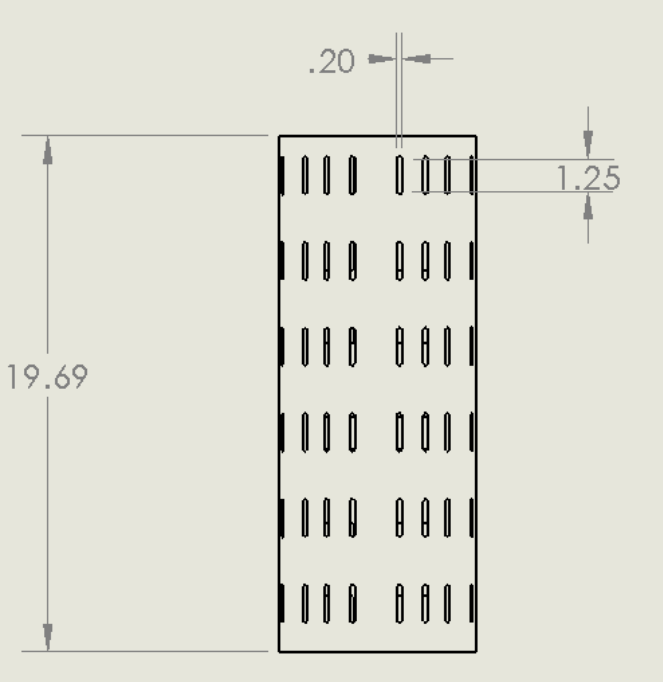

Figure 8. Side View of First Design Iteration (Inches)

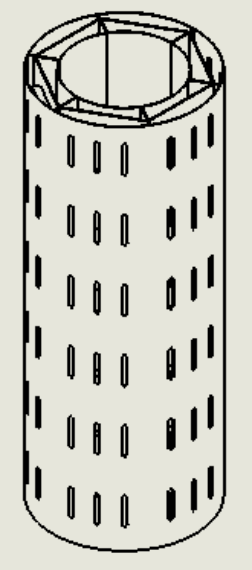

Figure 9. Isometric View of First Design Iteration

To further protect the thermoelectric modules from weather, we also designed a rain cap at the top of our device to protect the thermoelectric modules. Preventing water from entering the annulus of the device is crucial to the lifespan of the TEGs or else rusting will occur over time. Most rusting on an automobile will occur in the winter season due to the naturally harsh

conditions, so it is important to reduce exposure to the weather if our device was operated in New England (Washing Cars in Winter: How to Stop Rust on Cars, 2017). In this preliminary design stage, we positioned the rain cap and thermoelectric module to sit at the top of the exhaust pipe as shown in Figure 10. This was decided under the assumption that the heat transfer from the surface of the exhaust pipe at the outlet was less than the temperature near the inlet.

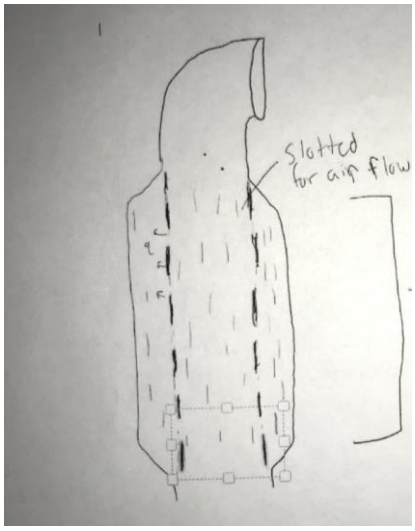

Figure 10. Hand Drawing of Device Positioned on the Exhaust Stack

Figure 11 shows the SOLIDWORKS model of the initial rain cap attached to our device. The rain cap was designed so as to protect precipitation from entering the top of the device while also still allowing exhaust gases to exit.

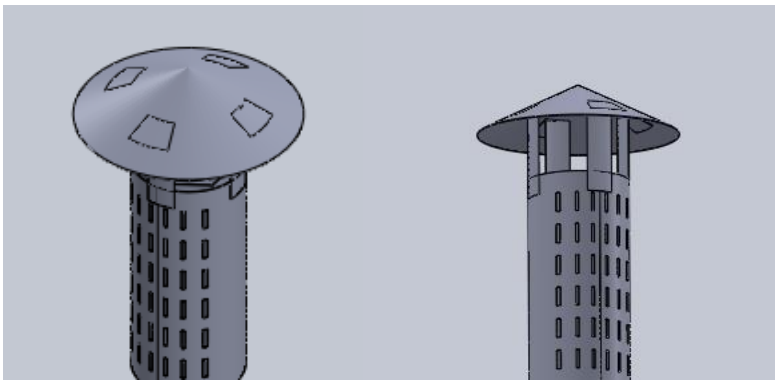

Figure 11. Preliminary Rain Cap Design

4.0 Final Design

Several changes were made to design a working and cost-effective prototype. For one, we had to consider the material properties and typical operating conditions of exhaust stacks in semi-trailer trucks. Exhaust stacks are typically around 6 inches in diameter and made of aluminized type 1 steel (TruckPipesUSA.com, 2020). We discovered that existing slotted cylindrical pieces of sheet metal surround the exhaust stacks as a safeguard to protect people from coming in direct contact with the hot surface. These heat shields are mandated in most states, so we decided to use these pre-existing heat shields to act as a form of protection for our module. The heat shield would prevent dust, rain, or any other small particulates from compromising the TEGs. This decision removes the cost of creating a custom slotted wall. Heat shields are also typically 10 inches in diameter (Iowa80.com, 2020). For our device, we designed its dimensions around a 6 inch exhaust stack that is 100 inches (2.54 meters) in length and a 10 inch heat shield (1.2192 meters) in length. Both the exhaust stack and heat shield are made of aluminized type 1 steel. With these constraints in mind, we designed the apothem length of the hexagonal wall of our device to be 3.55 inches. This distance was the best fit to achieve an optimal temperature gradient within the limitations of our TEGs. See Section 5.0 for the full dimensions of our device.

In the preliminary design, we decided to build the 0.5 meter device at the top of the exhaust stack. However, in an attempt to reduce the moment produced by our device and decrease the length of the wires needed, the device was moved to the bottom of the exhaust stack. The bottom of the hexagonal wall sits 4 inches away from the bottom of the exhaust stack. In this scenario, all rows of TEGs have a consistent temperature gradient and are not affected by any major turbulent wind coming from the opening at the bottom of the heat shield. The design of the rain cap was altered as seen in Section 4.2 to better fit within the heat shield. We also decreased the total length of our device from 0.5 meters to 0.3 meters and reduced the number of rows of TEGs to four instead of the preliminary five, still with one module per wall face. Therefore, the final design has a total of 24 TEG modules. The purpose in reducing the length of our device was to reduce the overall cost of the device.

The cost of our design had to be reasonable in comparison to the amount of electricity produced and the fuel cost savings anticipated for this project to prove feasible. The thermoelectric modules were the most costly element of this design, so reducing the number of

TEGs on the device not only reduced the upfront cost of the device, but made for easy installation and maintenance. See Section 8.0 for the cost analysis.

4.1 Hexagonal Wall

The purpose of the hexagonal wall was to provide a surface to mount the TEGs and to utilize the exhaust heat without having to exceed the maximum service temperature of the TEGs. The hexagonal wall remained the same shape and distance from the exhaust pipe and heat shield in all iterations of design. Several materials were considered for the wall that would fit our thermal and structural needs. When considering materials that would be suitable to mount our TEGs to, we were concerned with the service temperature, melting point, tensile strength, fracture strength, and thermal conductivity. The temperature of the exhaust gases at maximum engine load is 519℃, which is the temperature we considered the hexagonal wall should be able to withstand (Wang et al., 2014). A material with a low thermal conductivity seemed optimal at first to reduce the heat received by the TEGs which can operate continuously at a maximum of 250°C and only intermittently beyond 350°C (Hi-Z Technology, 2020). However, after software simulation, materials with a high thermal conductivity were considered as long as they fit the thermal requirements. The material used also needed to be structurally viable to fit on the exhaust stack of a semi-truck.

The materials considered for the hexagonal wall were Nickel-Cr-Co-Mo alloy-Rene 41, Zirconia (Y-TZP)(HIP), and aluminized type 1 steel. The aluminized steel is specifically Deep Drawing Steel (DDS) Ultra-Low Carbon ASTM A463 Aluminum-Coated Steel, Type I, Drawing Quality - DQHT Grade. Tables 1 and 2 list the material and thermal properties relevant to our project. The cost of these materials can be seen in Table 21 in Section 8.1.

Table 1: Key Material Properties (GRANTA; AK Steel, 2018; Harvey, 1982)

Material Description	Density $[kg/m^3]$	Young's Modulus [GPa]	Fatigue Strength at 10^7 Cycles [MPa]	Fracture Toughness $[MPa \cdot m^{0.5}]$	Tensile Strength [MPa]
Nickel-Cr-Co-Mo alloy, Rene 41	8250	220	620	91.6	1355
Zirconia (Y-TZP)(HIP)	6065	200	986	6.1	1125
Deep Drawing Steel (DDS) Ultra-Low Carbon ASTM A463 Aluminum-Coated Steel, Type I, Drawing Quality (DQHT Grade)	7870	200	278	73.8	310

Table 2: Key Thermal Properties (GRANTA; AK Steel, 2018; Harvey, 1982)

Material Description	Melting Point [℃]	Maximum Service Temperature [℃]	Thermal Conductivity [W/m℃]	Specific Heat Capacity [J/kg℃]
Nickel-Cr-Co-Mo alloy, Rene 41	1345	988.5	9	460
Zirconia (Y-TZP)(HIP)	2625	2030	2.95	427
Deep Drawing Steel (DDS) Ultra-Low CarbonASTM A463 Aluminum-Coated Steel, Type I, Drawing Quality (DQHT Grade)	1465	677	42-52	565-670

The hexagonal wall was originally designed to be 2 millimeters thick, the same thickness as the exhaust pipe and heat shield. After performing structural calculations (Section 6.0) of the different materials, we decided to reduce the thickness of the hexagonal to 0.762 millimeters (0.03 inches) as seen in Figure 12.

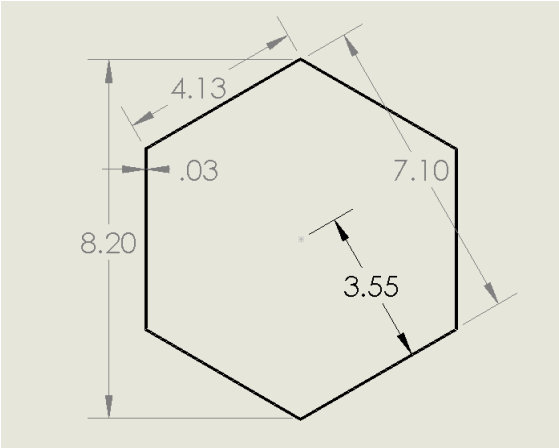

Figure 12. Top View of Hexagonal Wall (Inches)

The change in wall thickness reduces cost and weight. Table 3 below shows the weight of the 2 millimeter thickness is greater than the 0.762 millimeters thickness. The more material needed also increases the cost; the amount of material needed for the 0.762 millimeters is less than the amount needed for the 2 millimeters leading to a lower cost.

Table 3: Comparing Weights of Hexagonal Wall

Material	Weight [lbs] - 2 mm Thickness	Weight [lbs] - 0.762 mm Thickness
Nickel-Cr-Co-Mo alloy, Rene 41	7.004	2.650
Zirconia (Y-TZP)(HIP)	5.149	1.948
Deep Drawing Steel (DDS) Ultra-Low Carbon ASTM A463 Aluminum-Coated Steel, Type I, Drawing Quality (DQHT Grade)	6.682	2.528

Nickel-Cr-Co-Mo alloy and zirconia Y-TZP were first considered because they fit the initial specification of having a thermal conductivity less than 15 W/m℃. The thought behind this was that using a material with a thermal conductivity lower than that of stainless steel would reduce instances of hot spots and could increase temperature difference between either side of the TEG. Through the software simulations, later to be discussed, the nickel alloy had met the thermal requirements of maintaining a temperature below 250℃ and had exceeded requirements for most mechanical properties, because it had a higher strength than standard stainless steel. Upon further inspection of its mechanical properties, the nickel alloy was found to be too dense. With a hexagonal wall thickness of 2 millimeters, the nickel alloy weighed seven pounds by itself which was too heavy for our application (Table 3).

Zirconia was then considered due to its lower thermal conductivity in comparison to the nickel alloy, as well as its lower density, subsequently lowering its overall cost and weight (total of 5.15 pounds). Zirconia is a ceramic material that remains strong under the high service temperatures it would be experiencing. This material seemed promising with a fatigue strength of 986 MPa at 10^7 cycles (GRANTA). The maximum service temperature of zirconia Y-TZP is 2030℃, well above the expected 519℃ temperature from the semi-truck's exhaust stack (GRANTA). Zirconia's thermal conductivity of 2.95 W/m℃ is optimal to reduce the heat to the TEGs down to a safer operational temperature (GRANTA). It is important to note that zirconia Y-TZP has a bending strength of 1125 MPa, and the pressure from the structural support must not exceed these limits in the manufacturing process (GRANTA). Overall, this material appeared to pass all the requirements to be a worthy choice, however, the zirconia wall would weigh 5.149 pounds - not including the TEGs and supports - with the thickness needed for its mechanical properties. We ultimately determined zirconia Y-TZP's mechanical properties, specifically its fracture toughness of 6.1 $MPa \cdot m^{0.5}$, and its weight added to the stack, would not be sufficient for our design (GRANTA).

After much consideration, the finalized material for the hexagonal wall was ASTM A463 Aluminum-Coated Steel Type-I, Drawing Quality, also known as aluminized steel type 1 (DQHT Grade). The mechanical properties of aluminized steel can be obtained from its steel substrate. In the absence of certain steel substrate properties from the supplier, AK Steel, a low carbon steel of similar composition was used. YS500 low alloy steel properties were used to assess fatigue strength and fracture toughness of aluminized steel. This aluminum coated stainless steel

material is optimal for our design because of its weldability to the exhaust stack of the typical truck. The maximum service temperature of 677°C is above our maximum expected exhaust gas temperature of 519°C, which was a major factor for our design (AK Steel, 2018). The high melting point of the steel substrate, 1465°C, is desirable as it would operate within our temperatures without losing its strength (GRANTA). DQHT grade metal was chosen because it resists alloying of the aluminum coating up to 538°C (AK Steel, 2018). The material's thermal conductivity of 42-52 W/m°C was appealing for this application due to the need for a temperature difference (AK Steel, 2018). Aluminized steel type 1 has a tensile strength of 310 MPa, and a yield strength of 166 MPa, which was theoretically proven to be structurally sound when attached to the exhaust system (AK Steel, 2018; Section 6.0). The fatigue strength at 10^7 cycles for the steel substrate used to manufacture aluminized steel type 1 is 278 MPa. The maximum expected stress does not exceed this amount so failure due to fatigue is not a concern in this design.

An alternative option to using zirconia or type I aluminum-coated steel would be to use aluminum that has been processed by plasma electrolytic oxidation (PEO). PEO is an electrochemical surface treatment that is typically used to protect against corrosion and wear, and increasing hardness, however the properties of the resulting coating are dependent on the substrate that is used in the process and the electrolyte composition (Barik et. al., 2005). With the right treatment process, a lightweight aluminum alloy could be used instead which would reduce weight and be more resilient to weather conditions that might be encountered. However, an additional manufacturing process would increase the cost to create the device.

4.2 Rain Cap

The environment poses challenges to electronic systems, specifically the thermoelectric generators. A device mounted to the exterior of a semi-truck moving at high speeds through varying conditions must not only be able to withstand all types of weather, but also continue to function effectively through its intended lifetime to be considered a feasible tool. With our preliminary design as shown in Figure 11, a stainless steel rain cap was included at the top of the heat shield to protect the TEGs from rain and snow, as water damage would steadily deteriorate the quality of the TEGs. When the position of our device on the exhaust stack was changed, the rain cap was modified to the design shown in Figure 13.

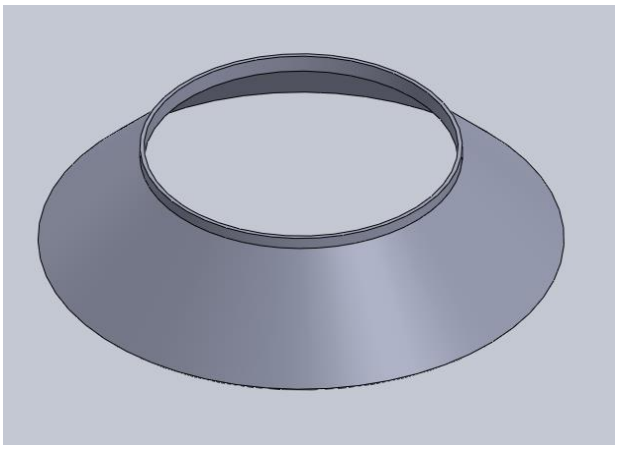

Figure 13. Rain Cap Model

This rain cap was designed to be 10.05 inches in diameter, fitting over the circumference of the heat shield. It was positioned so that the bottom of the cap sits 0.82 inches away from the top of the heat shield to allow for airflow while still providing adequate coverage. The rain cap in the final design was also changed from stainless steel to aluminized steel type 1 for better weldability with the aluminized steel exhaust stack. Figure 14 shows the rain cap relative to the entire assembly.

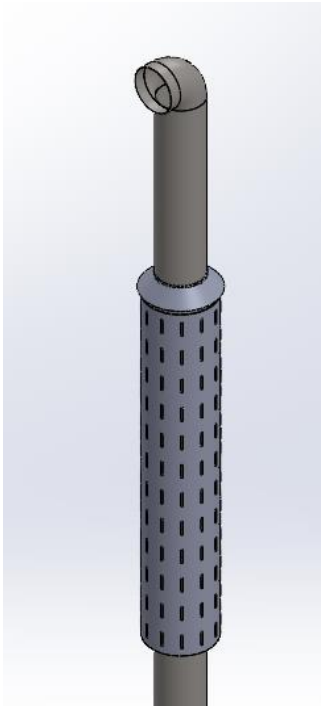

Figure 14. Rain Cap in Entire Assembly

Figures 15-17 show the dimensions of the final rain cap design.

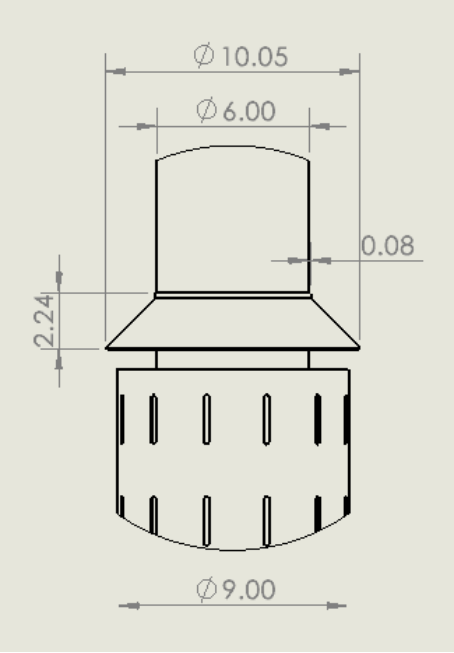

Figure 15. Final Rain Cap Design (Inches)

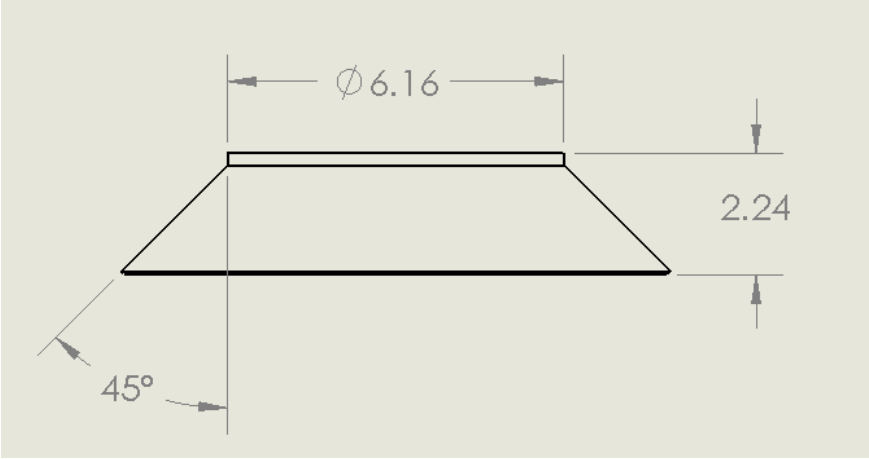

Figure 16. Side View of Rain Cap (Inches)

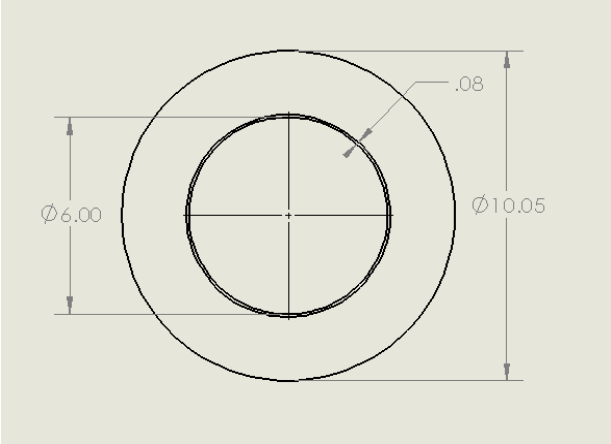

Figure 17. Top View of Rain Cap (Inches)

4.3 Support Structure

Our preliminary design included six stainless steel inner support structures that were supporting the hexagonal wall by attaching to the inner corners of the hexagonal wall (Figure 7). The support system in our preliminary design had potential weaknesses at the contact points of the exhaust stack and the hexagonal wall that would be exacerbated by the high temperatures expected. It would also prevent necessary cross flow around our device. With these, we designed an alternative support system that attaches to the pipe at six points and stabilizes the hexagonal wall from above and below (Figure 18). This structure was changed to aluminized steel type 1 so that it could be easily welded to the exhaust stack and reduce the variety of materials in the design, lowering the overall cost.

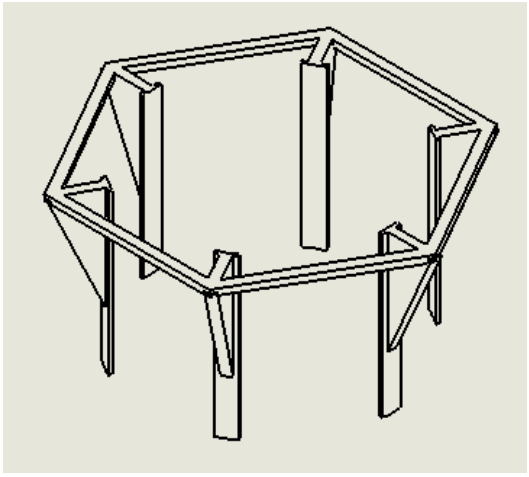
Figure 18. Support Structure for Hexagonal Wall

Figure 19 shows the top view and Figure 20 shows the front view of the supports.

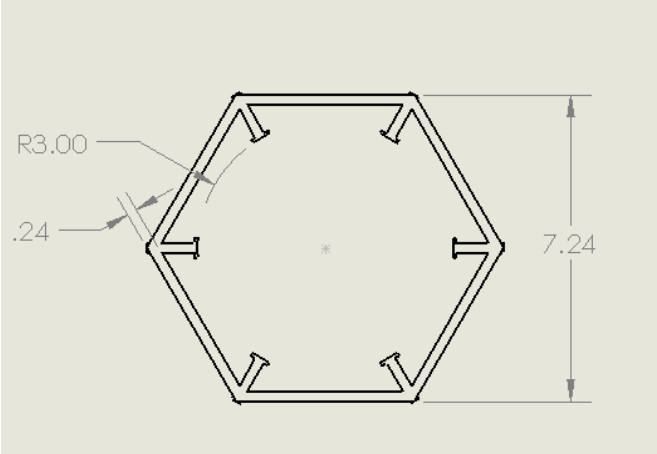

Figure 19. Top View of Supports (Inches)

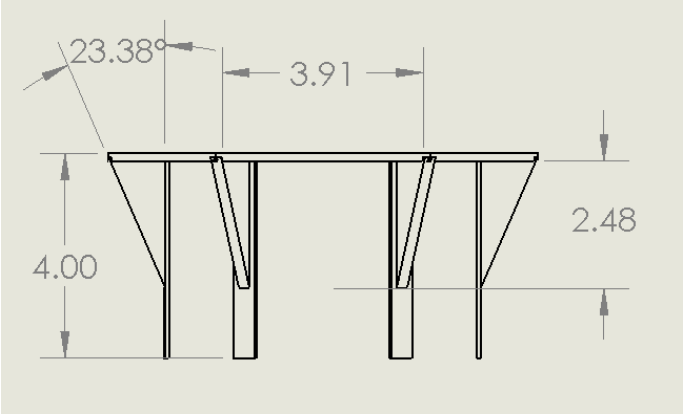

Figure 20. Front View of Supports (Inches)

4.4 Silicone Buffer

Silicone buffers were added for the hexagonal wall to connect to the top and bottom support structures. These buffers are to reduce the transfer of vibration and the friction between parts (Figure 21). Silicone rubber will absorb these vibrations and be able to withstand continuous use up to 260°C (GRANTA). As shown later in Section 7.3, the maximum predicted temperature of the hexagonal wall is 221.93°C. Rubber silicone also has the added benefit of being non-corrosive. This updated support system reduces heat transfer through contact and improves the structural integrity of the system by reducing mechanical vibrations and better dispersing the load of the device.

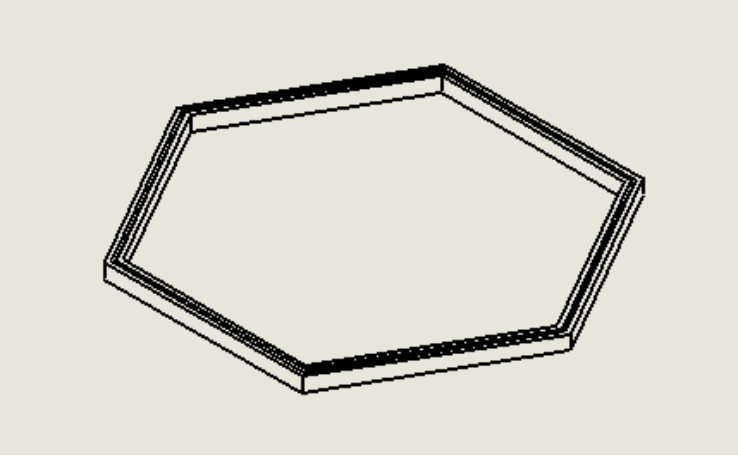

Figure 21. Silicone Buffer

Figure 22 shows the dimensions of the silicone buffer as top and side views.

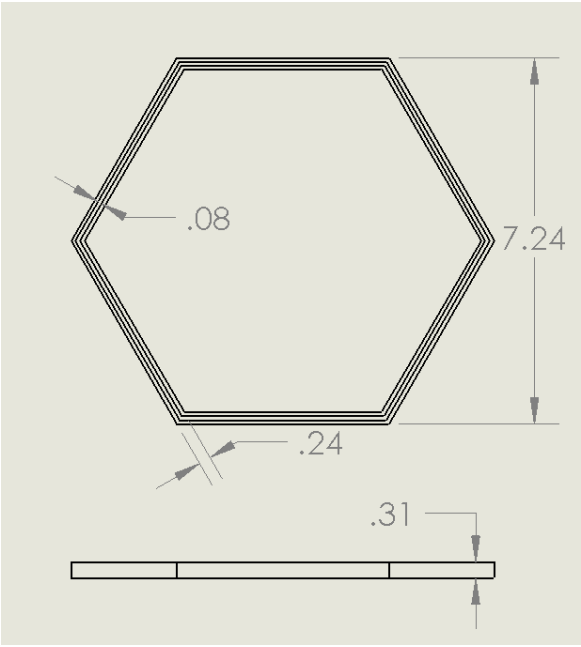

Figure 22. Top and Side View of Silicone Buffer (Inches)

5.0 Drawings and Assembly

Visuals of the final design are displayed in this section. Figure 23 shows the dimensions of the thermoelectric modules used (Hi-Z Technology, 2020).

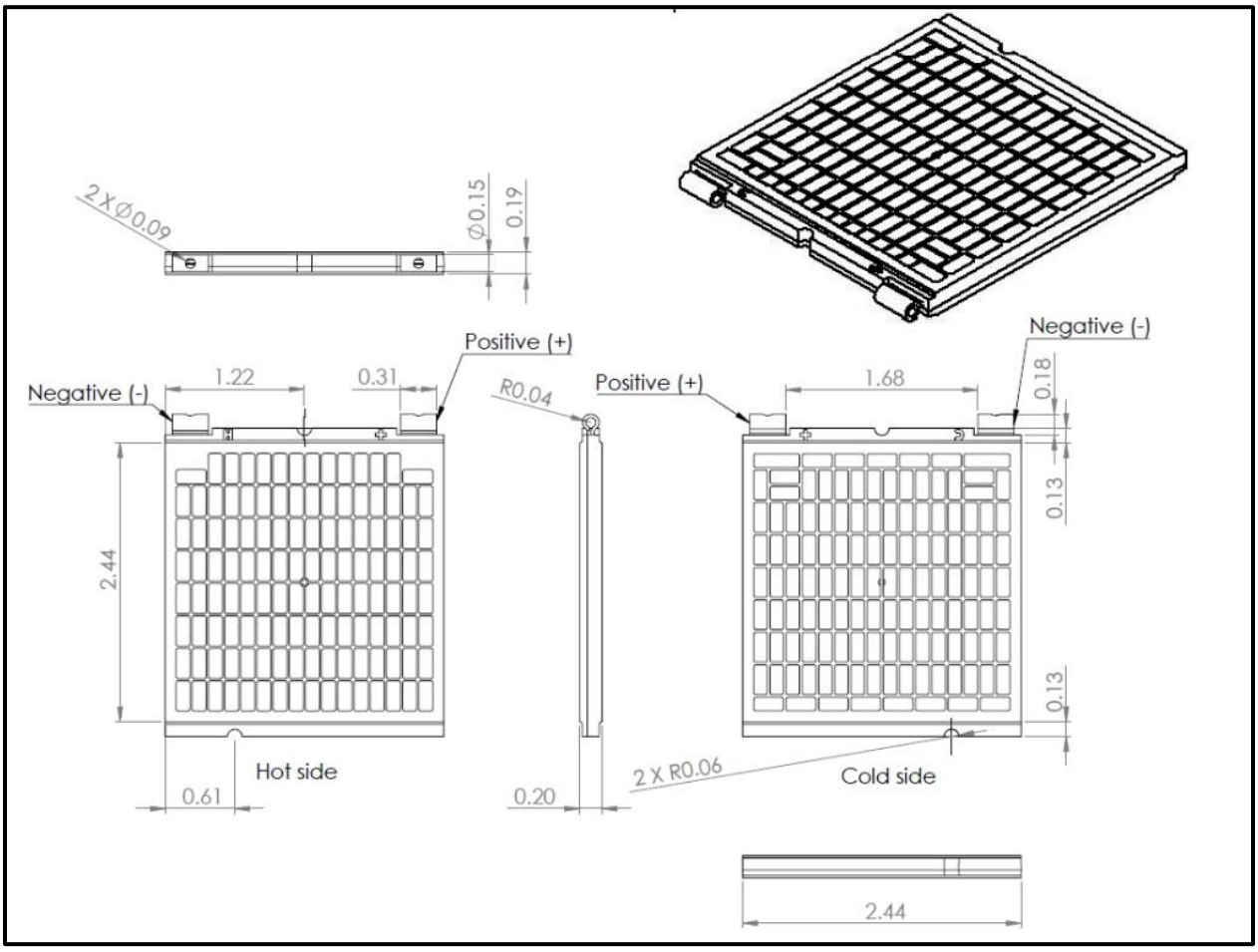

Figure 23. Dimensions for Thermoelectric Generator Module (Hi-Z Technology, 2020)

Figures 24-25 show the final iteration of the device and support structure assembled together.

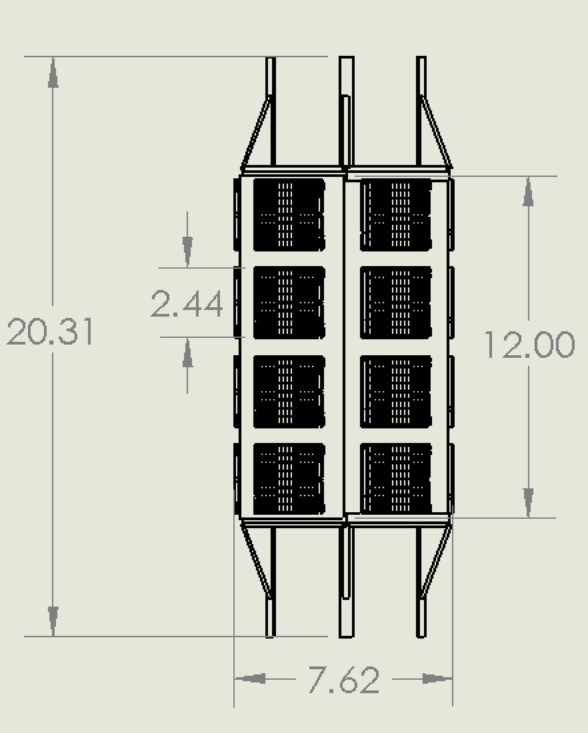

Figure 24. Front View of Design without Heat Shield (Inches)

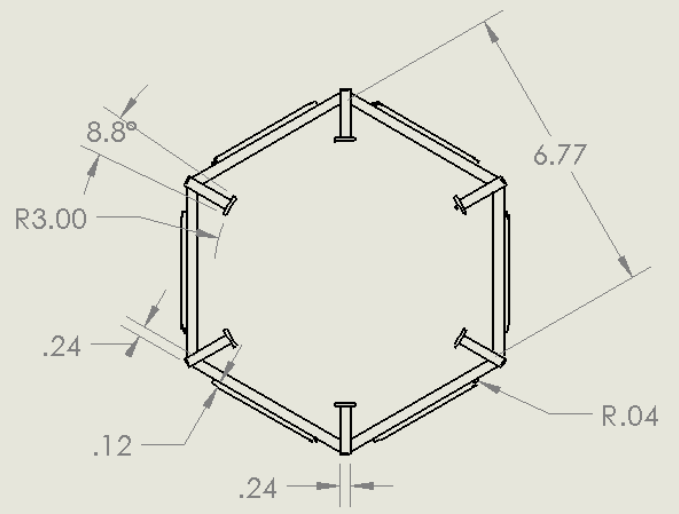

Figure 25. Top View of Design without Heat Shield (Inches)

Figure 26 shows a diagram of all the parts of our design except for the heat shield that encloses the entire assembly.

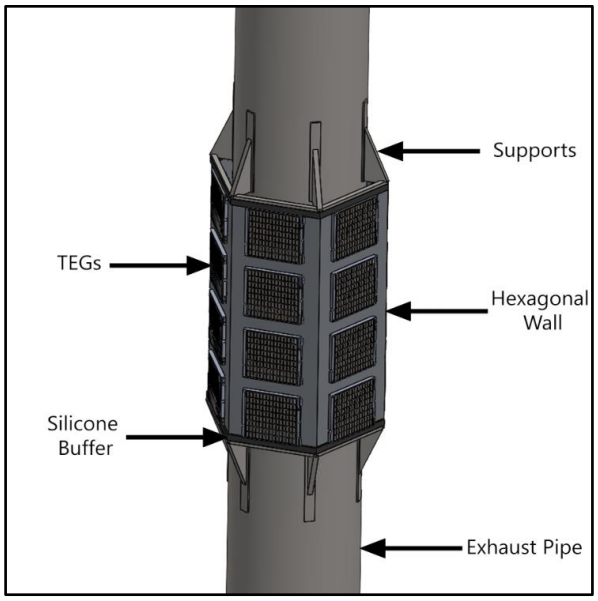

Figure 26. SOLIDWORKS Diagram of Parts Assembled in Final Design

Figure 27 shows the final design and full assembly placed on the exhaust stack of a semi-truck.

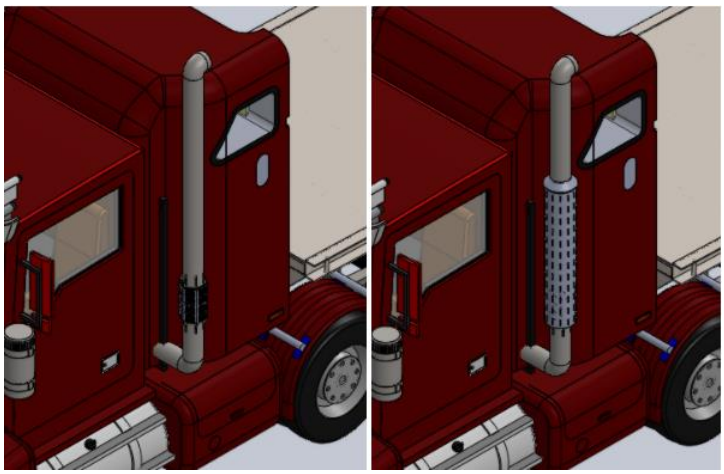

Figure 27. Thermoelectric Device Depicted on Semi-truck without Heat Shield (Left) and with Heat Shield and Rain Cap (Right)

6.0 Structural Analysis

A structural analysis of the stress and strain on our device was accomplished through theoretical calculations and finite element analyses using SOLIDWORKS and Ansys 2020.

6.1 Theoretical Calculations

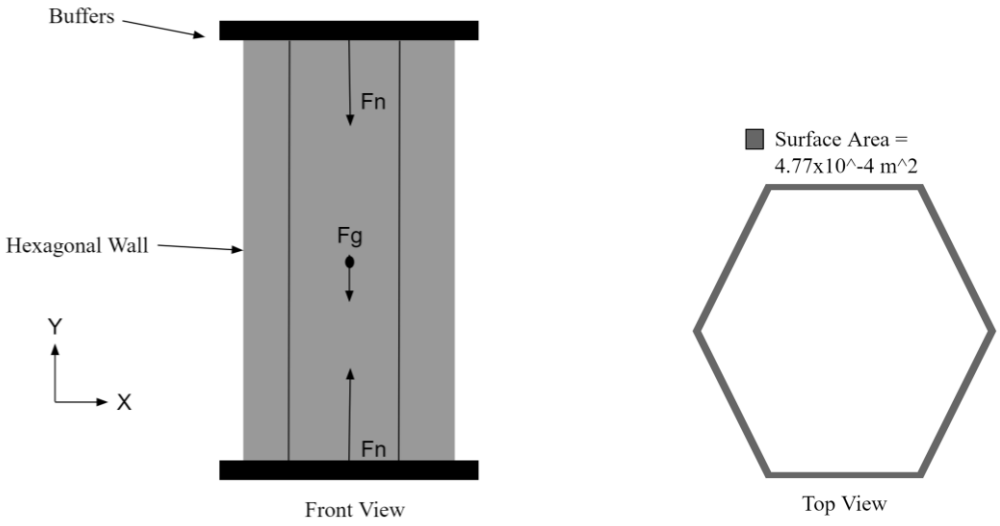

Figure 28. Free Body Diagram of Device

Figure 28 above shows the free body diagram of the device. The surface area is the cross-sectional area of the hexagonal wall with a thickness of 0.762 millimeters. The force of gravity and the compressive force on the hexagonal wall between the support structures were considered in the structural analysis of the hexagonal wall. The TEGs are not shown in this model, however, the force acting on the wall by the TEGs is fairly distributed, and is represented by adding the total weight of all TEGs to the weight of the hexagonal wall. The compressive force from the contact with the silicone buffers could vary in each installation depending on how much compressive force was applied when mounting the system to the exhaust stack. The 10 N of compressive force from the top support structure was used to secure the wall in place. This decision to add a small compressive force at the top of the wall was made because we need the supports on the top face of the hexagonal wall to press downwards to keep the wall in place within the silicone buffers. This force, in combination with the silicone buffer, would minimize

vibrations without causing significant deformation. Using equations for force (Equations 1-2), stress (Equation 3), and strain (Equation 4), the expected loads on the hexagonal wall were calculated.

The mass of the hexagonal wall, 1.147 kilograms, and the mass of the total 24 TEGs, 1.56 kilograms, were used to calculate the net force of gravity, F_g, which resulted in 26.5 N of force. The force in the y-direction was equal to the force of gravity plus the compressive 10 N force as expressed in Eq. 2 which equates to 36.5 N of force.

$$F_g = mg = (m_{wall} + m_{TEGs})g \quad \text{[Eq. 1]}$$

$$F_y = F_g + F_c \quad \text{[Eq. 2]}$$

The force of 36.5 N was used in Eq. 3 to find the stress on the hexagonal wall from compression which was calculated to be 7.65×10^{-2} MPa.

$$\sigma = \frac{F}{A} \quad \text{[Eq. 3]}$$

Hooke's Law, as shown in Eq. 4, was then used to calculate the strain with the compressive modulus of elasticity of aluminized steel (200 GPa) and the calculated stress (7.65×10^{-2}MPa).

$$\varepsilon = \frac{\sigma}{E} \quad \text{[Eq. 4]}$$

The strain was calculated to be 3.83×10^{-7}. The resulting stress values are less than that of the yield strength (166 MPa) of aluminized steel type 1 (AK Steel, 2018). See Appendix A for the entire calculations.

6.2 Simulation Results

SOLIDWORKS and Ansys were used to simulate the structural mechanics of the working device by inputting the loads derived from theoretical calculations. Both softwares predicted similar results for stress and strain. Additionally, the theoretical calculations were found to be within the ranges of stress and strain the software provided.

6.2.1 SOLIDWORKS

In SOLIDWORKS, a model of only the hexagonal wall and bottom support structure was analyzed because it can be assumed that the top support would not be receiving substantial amounts of stress relative to its bottom counterpart. The top support structure was not included in

the model in order to simplify the analysis. A distributed force of 36.5 N, the combined total force of gravity and compression, was applied to the top face of the hexagonal wall for this simulation. The results of the stress analysis are shown in Figure 29, which illustrate the range and distribution of stress and strain within our model.

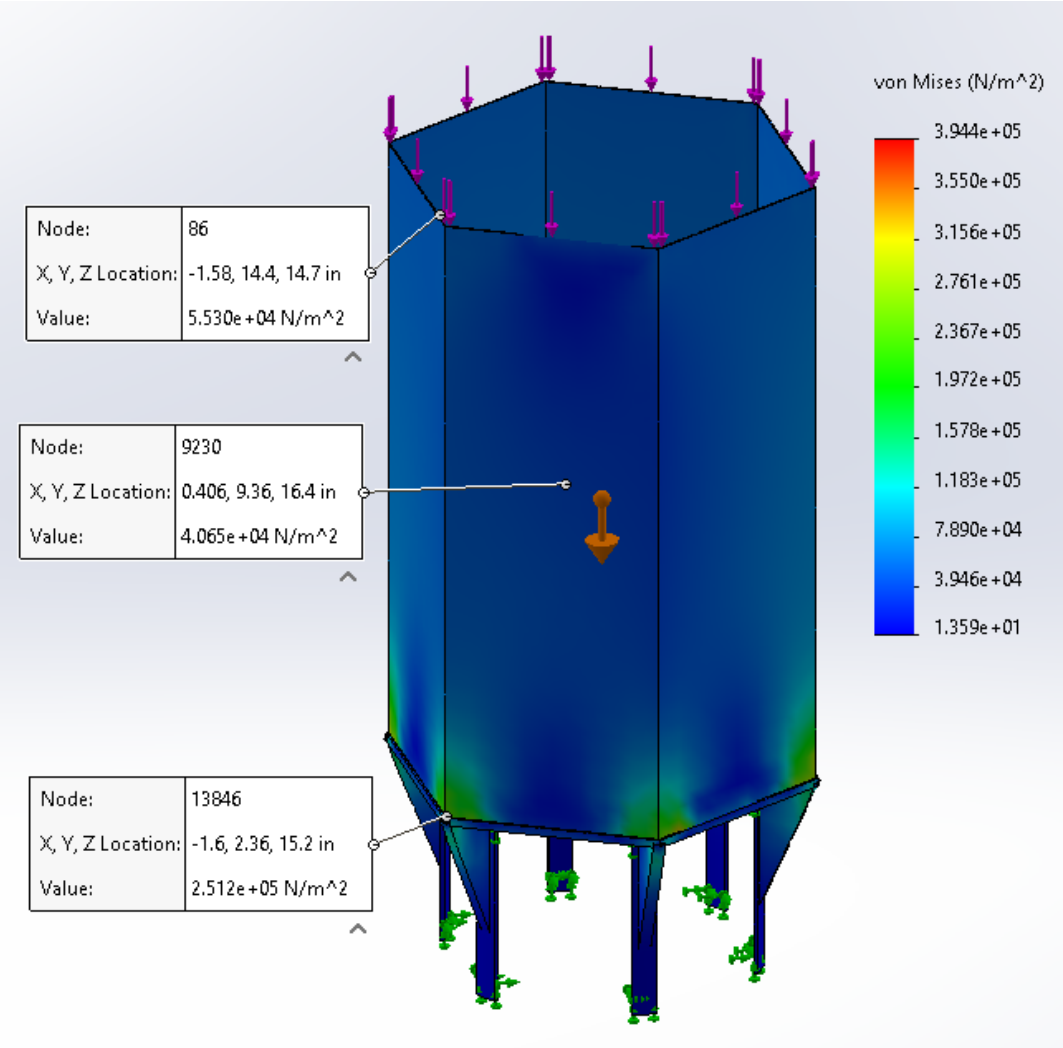

Figure 29. SOLIDWORKS Stress of Hexagonal Wall

The overall expected stress of 7.65×10^{-2}MPa from the theoretical calculations falls within the results of the SOLIDWORKS analysis (Figure 29). The maximum stress, 39.4×10^{-2}MPa, occurs at the corners where the hexagonal wall meets the support structure. The SOLIDWORKS analysis proves that our device is expected to experience stress less than the

yield strength (166 MPa) of aluminized steel (AK Steel, 2018). Figure 30 shows the results of strain.

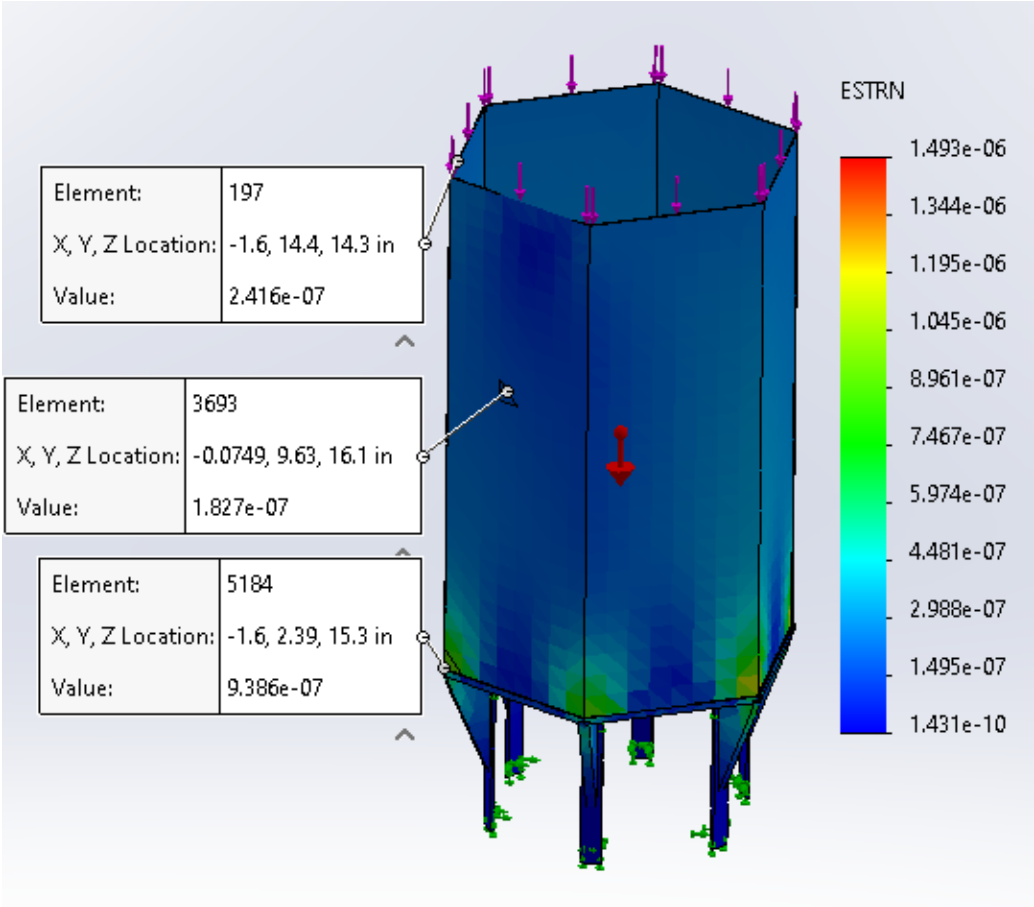

Figure 30. SOLIDWORKS Strain of Hexagonal Wall

The overall strain expected from the theoretical results, 3.83×10^{-7}, agrees with the simulated strain in Figure 30. Based on these results, the aluminized steel structures for the hexagonal wall and supports would not anticipate significant structural defects on the exhaust stack of a semi-truck.

In addition, the rain cap for the assembly was tested to ensure the edge weld would not deform from the force of gravity applied. Figure 31 shows the results of the expected stress.

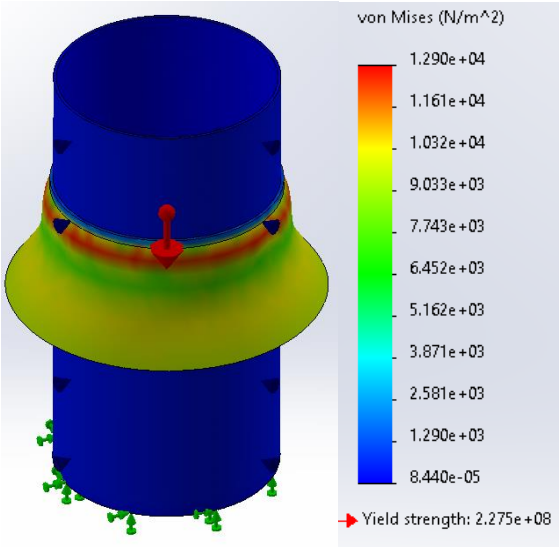

Figure 31. SOLIDWORKS Stress of Rain Cap

The maximum expected stress of the rain cap, 1.29 x 10^{-2} MPa, also proves to be within the limits of the material properties of aluminized steel. Figure 32 shows the results of the total deformation of the rain cap.

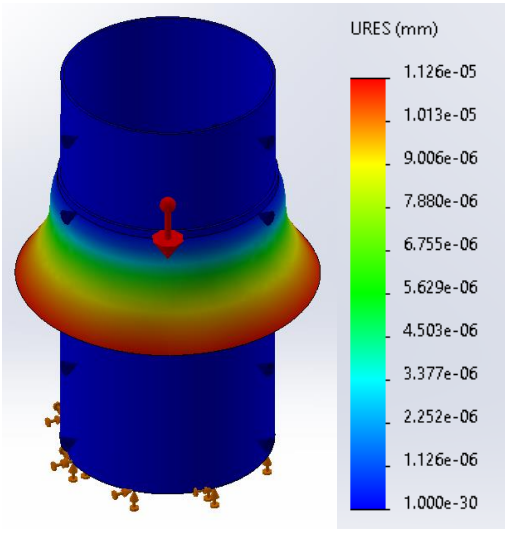

Figure 32. SOLIDWORKS Total Deformation of Rain Cap

The maximum total deformation is1.13×10^{-5}millimeters which is a very small deformation to be expected. This should be suitable for the expected environment of operation.

6.2.2 Ansys

The same model of the hexagonal wall and bottom support structure that was used in the SOLIDWORKS analysis was also used for the Ansys simulation. A total force of 36.5 N was applied to the top face of the hexagonal wall for consistency with the SOLIDWORKS structural analysis to account for the compressive force applied as well as the weight of the wall and the TEGs. Figure 33 shows the maximum expected stress of our design.

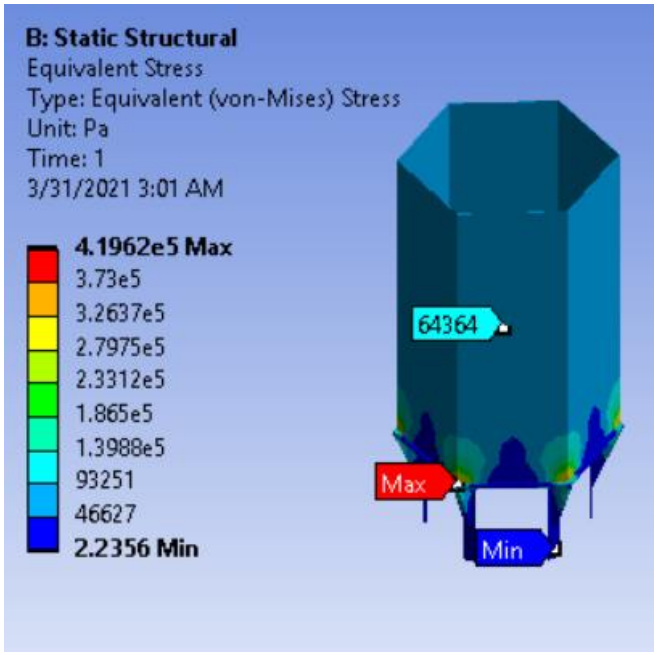

Figure 33. Ansys Stress Results

The maximum stress of this device is simulated to experience is 4.20×10^5 MPa, well below the of aluminized steel (310 MPa). Figure 34 shows the expected strain.

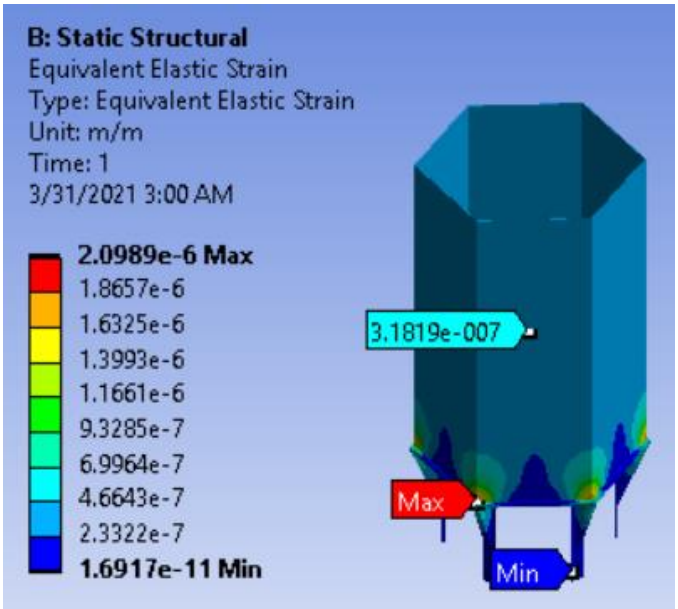

Figure 34. Ansys Strain Results

The expected maximum strain is 2.10×10^{-6}. These analyses suggest that the structure would be sufficient support for the TEGs to mount to without fear of failure within the exhaust stack's lifetime.

7.0 Thermal Analysis

To assess the theoretical power generating capabilities of the thermoelectric generator device, the conjugate heat transfer was theoretically calculated and then simulated in Ansys 2020. The values used in this analysis are based on a 6 cylinder, 4-stroke turbocharged diesel engine. This is the most common engine found in heavy duty vehicles such as semi-trucks. Our project is based on the diesel engine specifications listed in Table 4 (Wang et al., 2014). The results of the thermal analysis are based on the exhaust gases' inlet temperatures from Table 5 (Wang et al., 2014).

Table 4: Diesel Engine Specifications (Wang et al., 2014)

Bore [m]	Stroke [m]	Displacement $[cm^3]$	Compression Ratio	Injection Rail
0.126	0.130	6000	17:1	Common rail

Table 5: Inlet Parameters of Exhaust Gases (Wang et al., 2014)

Engine Load	25%	50%	75%	100%
Temperature [°C]	326	420	474	519
Mass Flow Rate [kg/s]	0.127	0.17	0.223	0.275

Tables 6 and 7 list the solid (AK Steel, 2018) and the fluid (Keenan et. al., 1984) material properties that were used in the thermal Ansys simulations. The properties of the exhaust gases in Table 7 were linearly interpolated at each respective engine load and temperature (Keenan et. al., 1984).

Table 6: Aluminized Steel Type 1 Thermal Properties for Ansys (AK Steel, 2018)

Temperature [K] and Engine Load	Specific Heat $[J/kg \cdot K]$	Thermal Conductivity $[W/m \cdot K]$
326℃ (25%)	565	52
420℃ (50%)	586	50
474℃ (75%)	628	45
519℃ (100%)	670	42

Table 7: Fluid Properties for Ansys Thermal Simulation (Keenan et al., 1984)

Fluid	Density $[kg/m^3]$	Specific Heat $[J/kg \cdot K]$	Thermal Conductivity $[W/m \cdot K]$	Dynamic Viscosity $[kg/m \cdot s]$	Prandtl Number
Air (20℃)	1.225	1007	0.02514	1.7804×10^{-5}	0.7309
Exhaust Gases (326℃)	0.590112	1062.76	0.045756	3.02084×10^{-5}	0.6936
Exhaust Gases (420℃)	0.50978	1073.8	0.05128	3.3226×10^{-5}	0.6955
Exhaust Gases (474℃)	0.4729	1086.76	0.0543	3.486×10^{-5}	0.6975
Exhaust Gases (519℃)	0.4465	1097.18	0.0567	3.61×10^{-5}	0.6995

Theoretical calculations of the thermal analysis were used to understand the basis of this heat transfer problem and to aid the computational fluid dynamics work in Ansys. Three dimensional and two dimensional models of the device simulated the heat transfer and convective cooling methods for a temperature difference across the thermoelectric generators.

7.1 Theoretical Calculations

The temperatures of the exhaust gases from inlet to outlet of the exhaust pipe were the main focus of the theoretical calculations. The exhaust gas conditions at 100% engine load were used to determine the maximum temperatures expected. The dimensions and thermal conductivity of the pipe were known, as well as the inlet temperature and mass flow rate of the exhaust gases. See Appendix H for the full calculations.

Using Equation 5, the velocity of the exhaust gases was calculated as 33.764 m/s.

$$V = \frac{\dot{m}}{\rho \cdot A} \quad \text{[Eq. 5]}$$

This velocity, along with the properties of air at 20°C (Table 7), and the inner diameter of the exhaust pipe (0.1524 m), were then used to solve for the Reynolds Number (Equation 6) of 63643.4. This proved the exhaust gases to be a fully turbulent flow.

$$Re_D = \frac{\rho V D_i}{\mu} \quad \text{[Eq. 6]}$$

Equations for friction factor (Equation 7) and Nusselt number (Equation 8) for fully turbulent flow were then used (Bergman, et al., 2011). Smooth walls can be assumed in this scenario because the roughness of aluminum is 2×10^{-6}meters (Engineering Toolbox, 2003). The Nusselt Number equation is validated because the Prandlt number of air at 20°C is 0.6995 (Keenan et al., 1984), the Reynolds Number is 63643.4, and Equation 9 is true.

$$f = (0.790 \ln Re_D - 1.64)^{-2} \quad \text{Turbulent, fully developed, smooth walls, } 3000 \lesssim Re_D \lesssim 5 \times 10^6 \quad \text{[Eq. 7]}$$

$$Nu_D = \frac{(f/8)(Re_D - 1000)\,Pr}{1 + 12.7(f/8)^{1/2}(Pr^{2/3} - 1)} \quad \text{Turbulent, fully developed, } 0.5 \lesssim Pr \lesssim 2000, \; 3000 \lesssim Re_D \lesssim 5 \times 10^6, \; (L/D) \gtrsim 10 \quad \text{[Eq. 8]}$$

$$\frac{L}{D_i} = \frac{2.54\ m}{0.1524\ m} = 16.667 \geq 10 \quad \text{[Eq. 9]}$$

The Nusselt number, 117.04, was then used to find the forced convective heat transfer coefficient (43.544 $W/m^2 \cdot K$) of the inner exhaust gases (Equation 10).

$$h_i = \frac{Nu_D \cdot k}{D_i} \quad \text{[Eq. 10]}$$

The temperature difference across the TEGs depends on forced air convection from normal vehicle operation. For the theoretical calculations, this external cross flow was calculated against the cylindrical exhaust stack. The hexagonal wall, TEGs, and heat shield were not

considered in this calculation because these parts had unknown wall temperature values that would be calculated via the Ansys simulations. The Reynolds Number of the cross flow, 93852.9, proved the external convective flow to be turbulent (Equation 11).

$$Re_D = \frac{\rho V D_o}{\mu} \quad \text{[Eq. 11]}$$

This Reynolds Number was then used in a Nusselt Number equation (Equation 12) for external cross flow over cylinders. The Nusselt Number was calculated as 244.796 and was used to find the outer, convective heat transfer coefficient (Equation 13), 39.3489 $W/m^2 \cdot K$ (Bergman et al., 2011).

$$Nu_D = 0.027 Re_D^{0.805} Pr^{1/3} \quad \text{[Eq. 12]}$$

$$h_o = \frac{Nu_D \cdot k}{D_o} \quad \text{[Eq. 13]}$$

Using all the known values and coefficients, the total heat transfer resistance was then calculated using Equation 14.

$$R_{tot} = \frac{1}{h_i \pi D_i L} + \frac{ln(D_o/D_i)}{2\pi k L} + \frac{1}{h_o \pi D_o L} \quad \text{[Eq.14]}$$

This R_{tot} was used in Equation 15 to solve for $T_{m,o}$, the temperature of the exhaust gases at the outlet. T_∞ was considered as 293 K.

$$\frac{T_\infty - T_{m,o}}{T_\infty - T_{m,i}} = \exp\left(-\frac{1}{\dot{m} c_p R_{\text{tot}}}\right) \quad \text{[Eq. 15]}$$

The calculated outlet temperature was 765.76 K. Using the calculated outlet temperature, the average temperature of the exhaust gases from inlet to outlet was calculated with Equation 16.

$$T_{Ave} = \frac{T_{m,i} + T_{m.o}}{2} \quad \text{[Eq. 16]}$$

The average theoretical temperature calculated was 778.88 K.

7.2 Simulation Results

3D and 2D models of the device were simulated in Ansys. The 3D model computed the hot-side temperatures of the thermoelectric generators while the 2D model computed the cold-side temperatures. The results of the temperature difference are in Section 7.3.

7.2.1 3D Model

A 3D simulation was used to calculate the temperatures of the hot side of the thermoelectric generators. This model included the exhaust pipe, hexagonal wall, and heat shield as shown in Figure 35. To simplify the analysis, the thermoelectric generators, the slots in the outer shield, and the structural supports were not modeled. The temperature at the hot side of the TEGs was calculated by simulating the heat transfer from the exhaust gases through the annulus between the exhaust pipe and hexagonal wall.

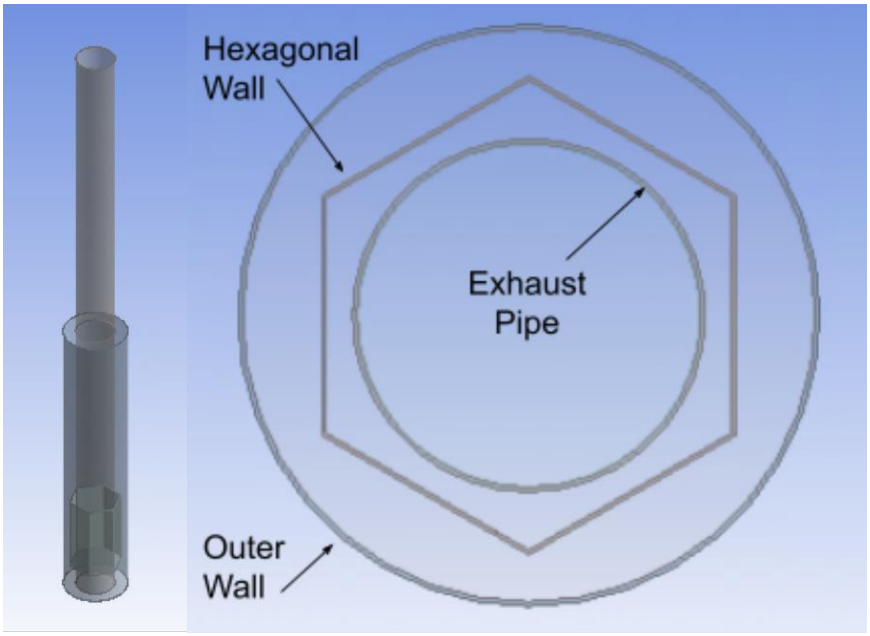

Figure 35. Geometry of 3D Ansys Model

The “Surface Integrals” report feature was used to find the temperatures calculated in the Ansys model. For a simulation at 100% engine load and the same conditions in the theoretical thermal calculations, the reported exhaust pipe outlet temperature was 769.44 K and the calculated result was 765.76 K (Section 7.1). The exact difference in results may be due to significant figures, but this proves that if the theoretical temperatures of the outlet and the average exhaust gases are similar to the results of Ansys, then the Ansys simulations for solving the TEGs’ hot side temperatures can be considered valid.

The 3D simulation focused on the hot side temperatures of the hexagonal wall where it would be in contact with the TEGs, assuming that there was uniform conduction across the

outside of the wall to the inside of the thermoelectric plate. The external forced convection was not included in the model because the 24 thermoelectric generators did not need to be included as long as their hot side temperature was assumed to be the same as the outside of the hexagonal wall. Four simulations were run in ambient conditions of 20℃ at 25%, 50%, 75%, and 100% engine load inlet conditions. It was assumed that there was constant heat transfer from the exhaust stack through the annuluses and hexagonal wall. See Appendix D for entire boundary conditions. Figure 36 shows the temperature colored contour results of the 3D model at 100% engine load.

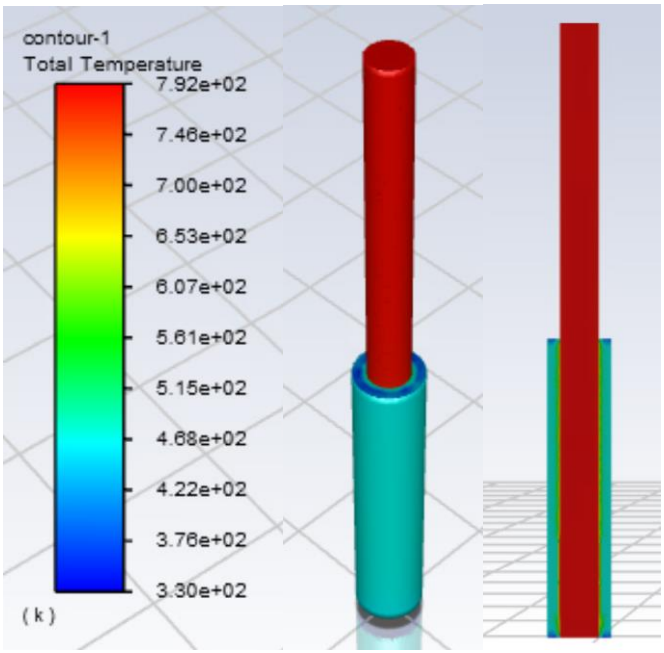

Figure 36. 3D Model Total Temperature Results Contour (Kelvin)

Figure 37 shows the colored contour results of the hexagonal wall part.

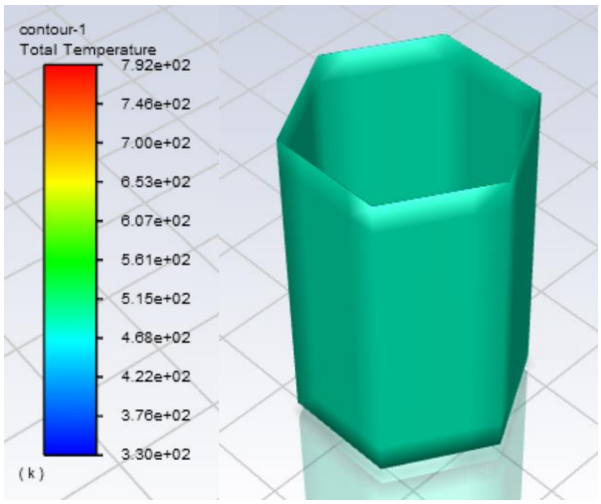

Figure 37. Hexagonal Wall Total Temperature Results Contour (Kelvin)

The “Surface Integrals” report feature was used to find the average temperature of the outside of the hexagonal wall, called “wall-hexagonal_wall-part_5-middle_air-shadow.” It was assumed that there was not a constant heat flux from the bottom of the hexagonal wall, closest to the exhaust pipe inlet, to the top of the wall. However, Ansys reported that there is a standard deviation of 1.068 K along the wall so the average wall temperature value was considered as the hot side temperature of all the TEGs across all four rows on the device. The temperature results of the hexagonal wall from the simulations at 25%, 50%, 75%, and 100% engine load are recorded in Section 7.3 as the hot side TEG temperature.

7.2.2 2D Model

The 2D model was focused on simulating the external forced convection and was simplified to a top down view. It simulated air flowing through the slotted heat shield that would cool the cold-side plates of the TEGs. In these simulations, the cold-side plate temperature was measured, which was needed to calculate the temperature difference and power output of the thermoelectric generators. The model geometry is shown in Figure 38.

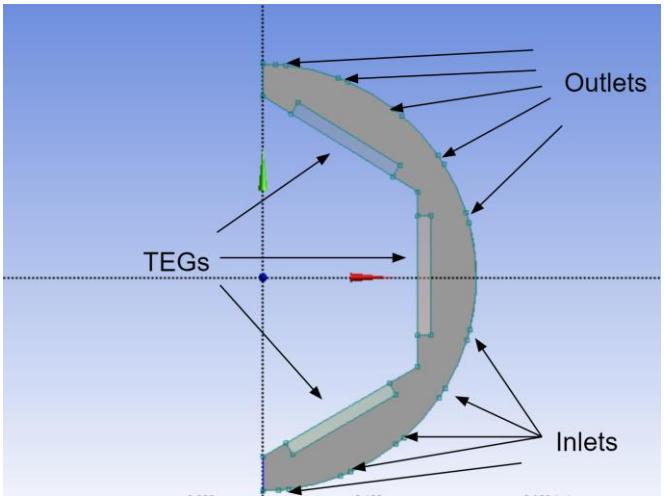

Figure 38. Geometry of 2D Ansys Model

As shown in Figure 38, only half of the system needed to be simulated. The air flow and temperatures of both sides would be very similar, so only half of the geometry was needed to achieve the desired results from the simulation. Also, as seen on the outer shell, five inlets and outlets evenly spaced were created to accurately represent the heat shield of the system. The setup for the 2D simulations started with the hexagonal wall. The temperature of this wall was set based on the 3D model. For example, the hot side temperature of the plate for 25% engine load at an ambient temperature of 20℃ was simulated in the 3D model. The result from that simulation was 434.44 K. This value was then used in the 2D simulation as a boundary condition for the hexagonal wall and TEG hot side temperatures. The next step in simulating the 2D model was setting the inlet velocities based on how fast the vehicle would be moving. These values were 20 MPH (8.94 m/s), 40 MPH (17.88 m/s), 60 MPH (26.83 m/s), and 80 MPH (35.76 m/s). The inlet air temperature was considered as 20°C for ambient environmental conditions as a standard temperature for our simulations.

The wall temperature of the outside cylinder or heat shield was set at 20°C - the same temperature as the ambient air. Note that the 20℃ wall temperature was not calculated, but the temperature change of it would not have significant effects on the cooling of the cold-side plates as proven by simulations. When the cylinder wall was raised to 350 K from 293 K for 20% engine load and ambient environment, the cold-side plate temperature was only raised by 0.8 K. The outlets were set at atmospheric pressure and the same temperature. Three TEGs were also included in this model, one on each side of the hexagonal wall. Under the assumption that there

is uniform conduction through the hexagonal wall and the hot-side plate of the TEG, the temperatures of the hot-side plates would experience the same temperature as the outside of the hexagonal wall. Also, the TEGs acted as conductors in this model due to the assumed uniform conduction of through the wall and to the TEGs. See Appendix E for the full boundary conditions and setup.

Figure 39 is an example of the wind velocity vectors flowing through the shell at a vehicle speed of 80 MPH and an engine load of 100%.

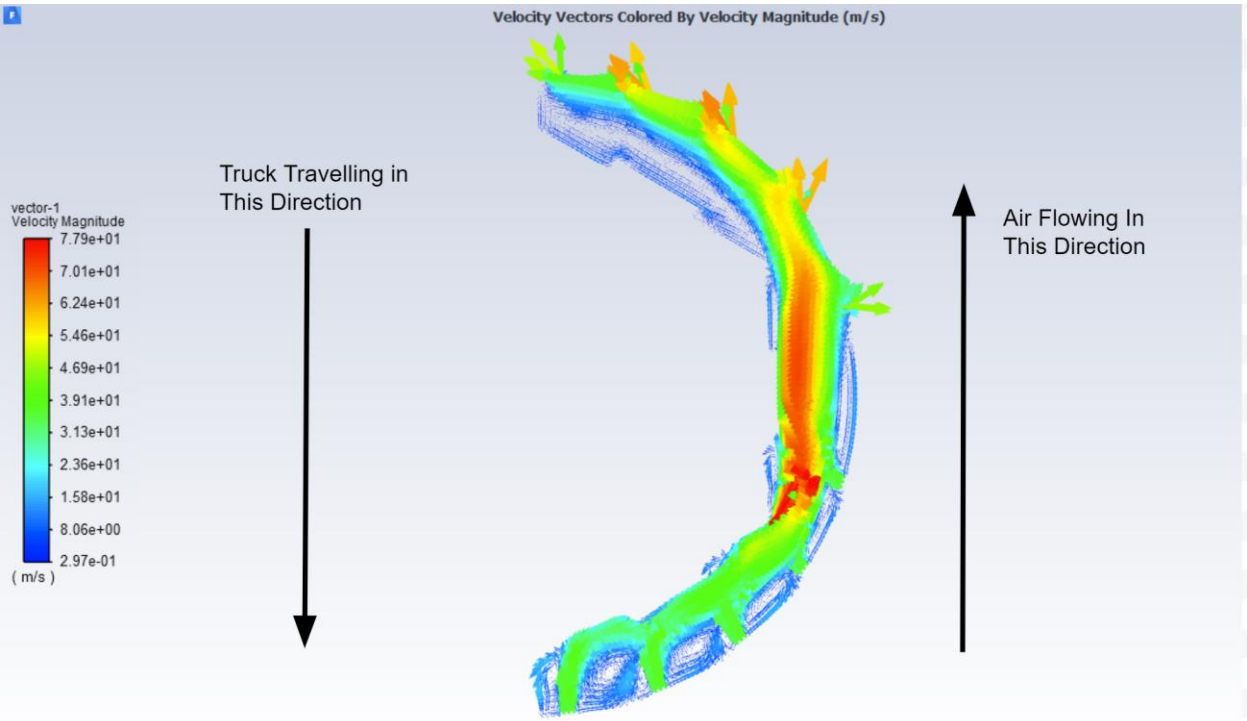

Figure 39. Velocity Vectors Within the Shell at 80 MPH and 100% Engine Load

As shown in Figure 39 above, there is air flowing through the shell from the vehicle moving. This simulation resembled a wind tunnel, where the air is controlled to flow in one direction. For this case, the semi-truck would be traveling in the direction shown in the Figure; the air would be flowing as shown and into the inlets in a magnitude and direction normal to the boundary. For this case, the maximum velocity vector is adjacent to the middle TEG. The back most TEG when looking at the front of the system (which is the uppermost TEG in Figure 38) is getting the least amount of air flow next to it. This TEG has the highest cooler-side plate temperature out of the three TEGs that were simulated. Since the temperature difference between

the bottom and top of the hexagonal wall is very low, the variance of cold temperatures would also be very low. This means it was assumed that if a TEG was selected on the row closest to the bottom of the exhaust stack, it would have an extremely similar cold-side plate temperature as a TEG from the row closest to the rain cap.

The highest cooler-side temperature was measured because it has the smallest temperature difference out of the TEGs. The smaller the temperature difference, the less power output and, in turn, a lower fuel cost savings. The results of these temperature differences and power outputs are displayed in Section 7.3. Selecting the smallest temperature difference means that the minimum cost savings out of all the TEGs was considered and calculated. To measure the temperature of the cold side of the TEG, a line was created along the outermost wall of the TEG acting as an arbitrary surface as seen in Figure 40. The average temperature along this line was calculated with the "Surface Integrals" report feature in Ansys.

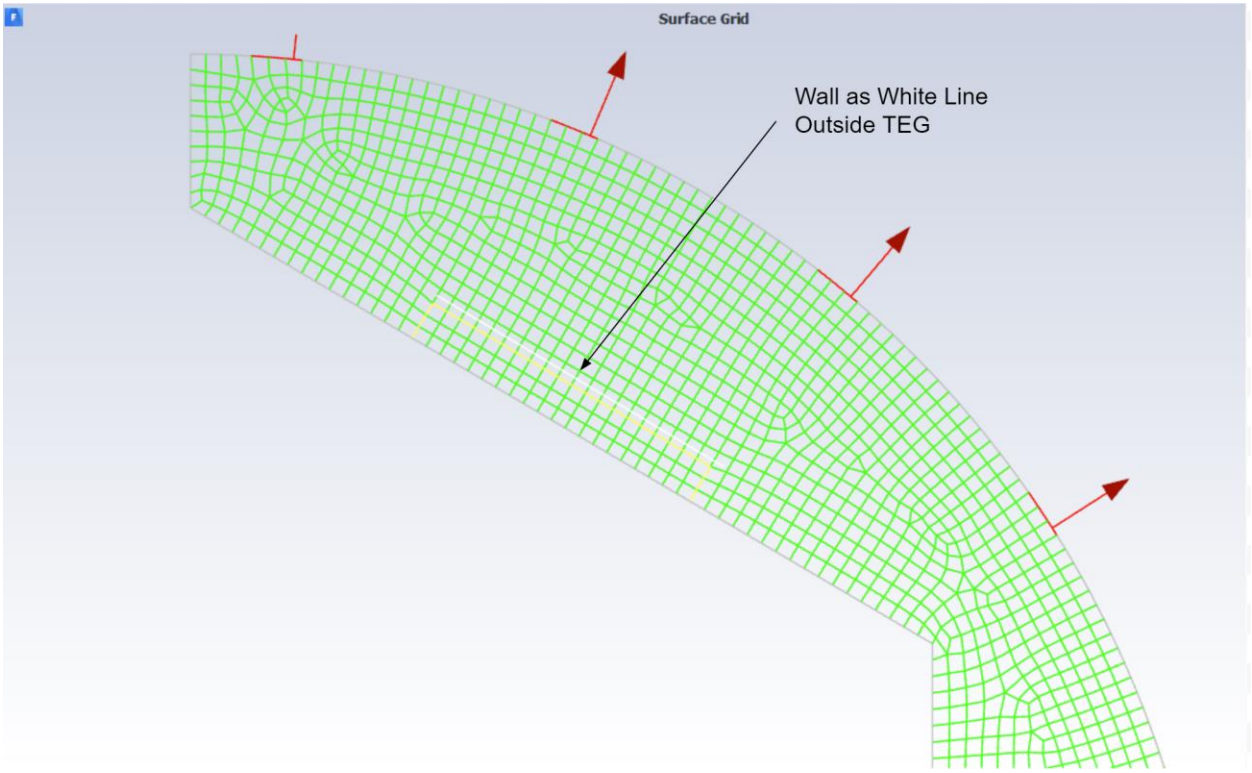

Figure 40. Mesh of Arbitrary Surface as Line to Measure TEG Cooler-Side Plate

The contour map, Figure 41, showed the range of temperatures for the system for ambient conditions and 20 MPH.

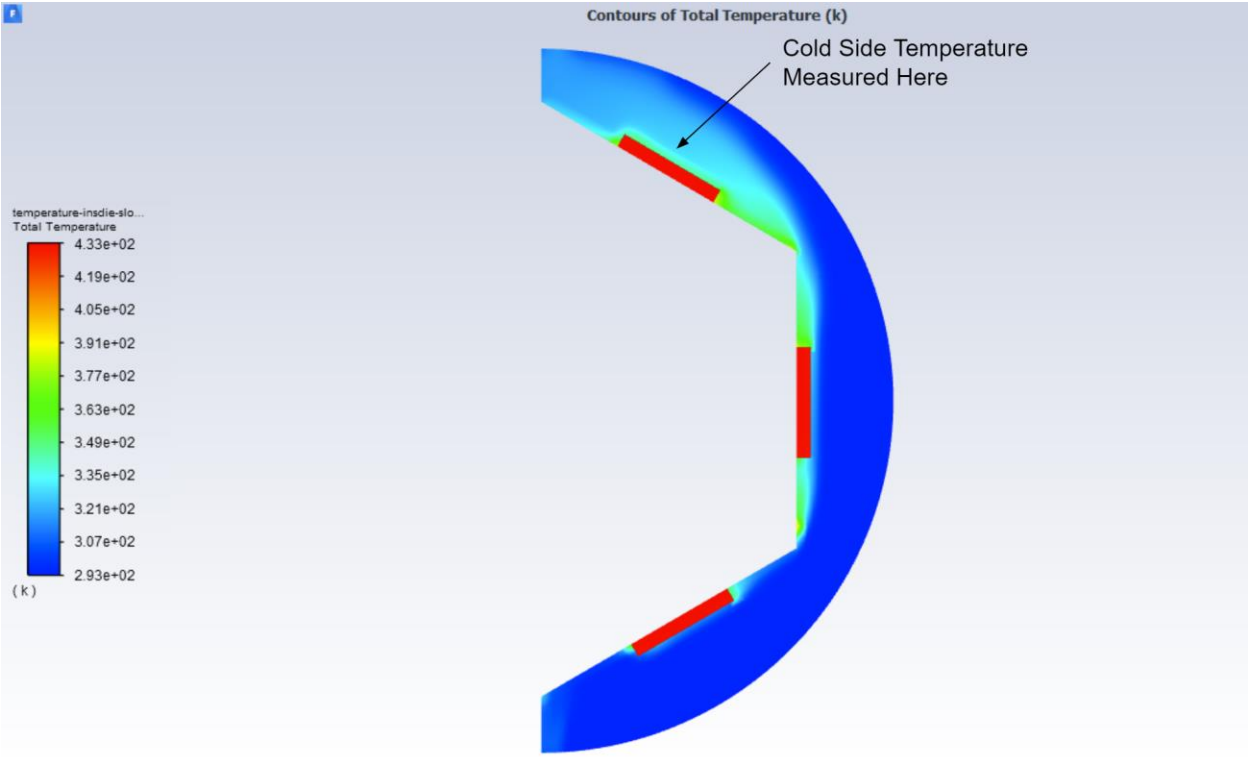

Figure 41. Contour Color Map of Cooler Side Temperatures

To simulate the 2D model, a number of assumptions had to be made. The first was that the hot side plate of the TEGs was the same temperature as the hexagonal wall. This was assumed due to the fact that the TEGs are attached directly on the wall and conduction is uniform through the hexagonal wall and hot-side plate of the TEGs. Another assumption made to simulate the model was that the two TEGs not measured would have a greater temperature difference and higher power output. The cooler-side plates of those TEGs would not be measured due to the fact that they would generate more cost savings than what was measured on the hot-side. This would provide a more conservative estimate for return. The two TEGs not measured had more airflow around the cooler-side plates than the TEG measured as shown by the velocity vector figure (Figure 39). This means that the cooler-side plates would be at lower temperatures for those TEGs compared to the TEG measured. It was then decided that those two TEGs would be viable if the TEG measured was also viable.

A concern that needs to be addressed with this design are hotspots. As shown in the contour results (Figure 39) there are spots along the hexagonal wall that have less airflow around

them relative to the rest of the shell. These areas are higher in temperature and were considered to be hotspots. More areas where hotspots would be are the faces of the hexagonal wall where the TEGs are connected. These are areas where heat transfer cannot occur easily and a build up of heat can happen. The hotspots can lead to the materials of both the wall and TEGs to have a shorter lifespan due to the extra heat for prolonged periods of time in these areas. The hotspots within our system are not extreme as along those areas where there is less air flow, the temperatures range from 340 K to 400 K depending on the conditions. This was calculated in the simulations. These may not have a significant impact, but they should be considered when assessing the longevity of the system. Another issue to note is that the thermal resistances of the TEGs were neglected in this model. The resistances were neglected due to creating a more basic thermal analysis. Although they were neglected in this model, the thermal resistances of TEGs are existent. To further advance this model, these resistances should be included, and this will give insight into whether there are severe hotspots where the TEGs are attached.

As mentioned previously, the TEG farthest back when facing the front of the vehicle is the TEG with the greatest temperature difference from our simulations. There were some restrictions to the 2D and 3D models that should be noted. The first was that the TEGs were simplified to one solid body rather than two semi-conducting plates which would be more realistic in the operation of TEGs. Another restriction was that the measured temperatures were approximated and could be different when tested in a real world scenario. Finally, the exhaust stack is expected to undergo turbulence, which causes uncertainty in the software due to its unpredictable nature. This uncertainty is more apparent due to the 2D and 3D models being separate simulations.

7.3 Temperature Difference Results

Tables 8-11 summarize the results of the 2D and 3D Ansys simulations as the hot and cold side temperatures of the TEGs with ambient conditions of 20℃.

The TEG temperature difference was then calculated and used to determine the power output and efficiency of one TEG module based on Figures 3 and 4, the data graphs provided by Hi-Z Technology (See Section 9.2 for how the power output and efficiencies values were obtained). The total power output of our device was calculated by multiplying the power output per one TEG by the total 24 TEGs.

Table 8: Ambient Conditions of 20°C with Vehicle Speed of 20 MPH

Engine Load	Hot Side Temperature [K]	Hot Side Temperature [°C]	Cold Side Temperature [K]	Cold Side Temperature [°C]	Temperature Difference [K or °C]	Power Output per 1 TEG Module [W]	Total Power Output [W]	TEG Efficiency [%]
25%	434.44	161.44	348.14	75.14	86.3	3.64	87.36	1.99
50%	462.66	189.66	358.99	85.99	103.67	4.83	115.92	2.3
75%	475.56	202.56	363.9	90.9	111.66	5.4	129.6	2.32
100%	487.49	214.49	368.44	95.44	119.05	6.03	144.72	2.46

Table 9: Ambient Conditions of 20°C with Vehicle Speed of 40 MPH

Engine Load	Hot Side Temperature [K]	Hot Side Temperature [°C]	Cold Side Temperature [K]	Cold Side Temperature [°C]	Temperature Difference [K or °C]	Power Output per 1 TEG Module [W]	Total Power Output [W]	TEG Efficiency [%]
25%	434.44	161.44	341.72	68.72	92.72	4.24	101.76	2.18
50%	462.66	189.66	351.29	78.29	111.37	5.6	134.4	2.47
75%	475.56	202.56	355.63	82.63	119.93	6.41	153.84	2.58
100%	487.49	214.49	359.67	86.67	127.82	7.03	168.72	2.68

Table 10: Ambient Conditions of 20°C with Vehicle Speed of 60 MPH

Engine Load	Hot Side Temperature [K]	Hot Side Temperature [°C]	Cold Side Temperature [K]	Cold Side Temperature [°C]	Temperature Difference [K or °C]	Power Output per 1 TEG Module [W]	Total Power Output [W]	TEG Efficiency [%]
25%	434.44	161.44	338.85	65.85	95.59	4.51	108.24	2.25
50%	462.66	189.66	347.9	74.9	114.76	6.07	145.68	2.55
75%	475.56	202.56	351.98	78.98	123.58	6.86	164.64	2.68
100%	487.49	214.49	355.78	82.78	131.71	7.51	180.24	2.78

Table 11: Ambient Conditions of 20°C with Vehicle Speed of 80 MPH

Engine Load	Hot Side Temperature [K]	Hot Side Temperature [°C]	Cold Side Temperature [K]	Cold Side Temperature [°C]	Temperature Difference [K or °C]	Power Output per 1 TEG Module [W]	Total Power Output [W]	TEG Efficiency [%]
25%	434.44	161.44	337.01	64.01	97.43	4.62	110.88	2.28
50%	462.66	189.66	345.69	72.69	116.97	6.31	151.44	2.6
75%	475.56	202.56	349.59	76.59	125.97	7.07	169.68	2.73
100%	487.49	214.49	353.23	80.23	134.26	7.79	186.96	2.84

The results show that both the TEGs and hexagonal wall were cooled when the vehicle is in motion. The greater the wind speed, the cooler those temperatures were. This is shown throughout the simulations as the maximum temperature measured was 95.44°C at 20 MPH and the lowest measured temperature was 64.01°C at 80 MPH. These temperatures were also measured at the lowest engine load. It is shown that the largest temperature differences, and therefore largest power outputs, are from the 75% and 100% engine loads as shown in Tables 8-

11. The maximum power output, 186.96 Watts, resulted from 100% engine load conditions and a vehicle speed of 80 MPH.

Although an ambient temperature of 20°C is considered our standard, it is not the most realistic. If this MQP had been built, our device would have been tested in Massachusetts climate conditions. To simulate the results of our device in more realistic conditions, average monthly temperatures in Massachusetts were considered for the system surroundings. The month of January had the lowest average temperature, -6.95°C, and July had the highest average temperature, 32.2°C, so the environmental temperatures of these months were simulated in the 3D and 2D Ansys simulations (weather-us, 2021). These temperatures each replaced the boundary conditions in the 3D and 2D models that were previously 20°C or 293K. The simulations and temperature results repeated the same process as for ideal conditions of 20°C. Table 12-15 are the results of the temperature differences in January.

Table 12: January Conditions with Vehicle Speed of 20 MPH

Engine Load	Hot Side Temperature [K]	Hot Side Temperature [°C]	Cold Side Temperature [K]	Cold Side Temperature [°C]	Temperature Difference [K or °C]	Power Output per 1 TEG Module [W]	Total Power Output [W]	TEG Efficiency [%]
25%	419.95	146.95	325.92	52.92	94.03	4.35	104.4	2.27
50%	447.14	174.14	336.36	63.36	110.78	5.89	141.36	2.54
75%	459.44	186.44	341.08	68.08	118.36	6.48	155.52	2.65
100%	471.04	198.04	345.49	72.49	125.55	7.14	171.36	2.76

Table 13: January Conditions with Vehicle Speed of 40 MPH

Engine Load	Hot Side Temperature [K]	Hot Side Temperature [°C]	Cold Side Temperature [K]	Cold Side Temperature [°C]	Temperature Difference [K or °C]	Power Output per 1 TEG Module [W]	Total Power Output [W]	TEG Efficiency [%]
25%	419.95	146.95	318.96	45.96	100.99	5	120	2.44
50%	447.14	174.14	328.21	55.21	118.93	6.76	162.24	2.76
75%	459.44	186.44	332.34	59.34	127.1	7.44	178.56	2.87
100%	471.04	198.04	336.24	63.24	134.8	8.22	197.28	2.99

Table 14: January Conditions with Vehicle Speed of 60 MPH

Engine Load	Hot Side Temperature [K]	Hot Side Temperature [°C]	Cold Side Temperature [K]	Cold Side Temperature [°C]	Temperature Difference [K or °C]	Power Output per 1 TEG Module [W]	Total Power Output [W]	TEG Efficiency [%]
25%	419.95	146.95	315.86	42.86	104.09	5.3	127.2	2.51
50%	447.14	174.14	324.57	51.57	122.57	7.2	172.8	2.84
75%	459.44	186.44	328.46	55.46	130.98	7.9	189.6	2.97
100%	471.04	198.04	332.14	59.14	138.9	8.81	211.44	3.11

Table 15: January Conditions with Vehicle Speed of 80 MPH

Engine Load	Hot Side Temperature [K]	Hot Side Temperature [°C]	Cold Side Temperature [K]	Cold Side Temperature [°C]	Temperature Difference [K or °C]	Power Output per 1 TEG Module [W]	Total Power Output [W]	TEG Efficiency [%]
25%	419.95	146.95	313.85	40.85	106.1	5.51	132.24	2.56
50%	447.14	174.14	322.21	49.21	124.93	7.45	178.8	2.88
75%	459.44	186.44	325.93	52.93	133.51	8.32	199.68	3.04
100%	471.04	198.04	329.46	56.46	141.58	9.17	220.08	3.18

The smallest expected temperature difference is 94.03°C at 25% engine load and moving at 20 MPH. A total power output of 104.4 Watts is produced and the efficiency of the TEGs at this temperature is 1.83%. The highest temperature difference, 141.58°C, occurs at 100% engine load and 80 MPH.

Table 16-19 are the results of the device in July.

Table 16: July Conditions with Vehicle Speed of 20 MPH

Engine Load	Hot Side Temperature [K]	Hot Side Temperature [°C]	Cold Side Temperature [K]	Cold Side Temperature [°C]	Temperature Difference [K or °C]	Power Output per 1 TEG Module [W]	Total Power Output [W]	TEG Efficiency [%]
25%	441.01	168.01	358.18	85.18	82.83	3.26	78.24	1.89
50%	469.68	196.68	369.22	96.22	100.46	4.25	102	2.16
75%	482.85	209.85	374.24	101.24	108.61	4.9	117.6	2.1
100%	494.93	221.93	378.84	105.84	116.09	5	120	2

Table 17: July Conditions with Vehicle Speed of 40 MPH

Engine Load	Hot Side Temperature [K]	Hot Side Temperature [°C]	Cold Side Temperature [K]	Cold Side Temperature [°C]	Temperature Difference [K or °C]	Power Output per 1 TEG Module [W]	Total Power Output [W]	TEG Efficiency [%]
25%	441.01	168.01	352.01	79.01	89	3.87	92.88	2.04
50%	469.68	196.68	361.78	88.78	107.9	5.08	121.92	2.34
75%	482.85	209.85	366.21	93.21	116.64	5.87	140.88	2.45
100%	494.93	221.93	370.27	97.27	124.66	6.52	156.48	2.54

Table 18: July Conditions with Vehicle Speed of 60 MPH

Engine Load	Hot Side Temperature [K]	Hot Side Temperature [°C]	Cold Side Temperature [K]	Cold Side Temperature [°C]	Temperature Difference [K or °C]	Power Output per 1 TEG Module [W]	Total Power Output [W]	TEG Efficiency [%]
25%	441.01	168.01	349.28	76.28	91.73	4.12	98.88	2.12
50%	469.68	196.68	358.45	85.45	111.23	5.44	130.56	2.42
75%	482.85	209.85	362.62	89.62	120.23	6.24	149.76	2.52
100%	494.93	221.93	366.47	93.47	128.46	6.88	165.12	2.62

Table 19: July Conditions with Vehicle Speed of 80 MPH

Engine Load	Hot Side Temperature [K]	Hot Side Temperature [°C]	Cold Side Temperature [K]	Cold Side Temperature [°C]	Temperature Difference [K or °C]	Power Output per 1 TEG Module [W]	Total Power Output [W]	TEG Efficiency [%]
25%	441.01	168.01	347.49	74.49	93.52	4.29	102.96	2.18
50%	469.68	196.68	356.3	83.3	113.38	5.7	136.8	2.46
75%	482.85	209.85	360.32	87.32	122.53	6.47	155.28	2.59
100%	494.93	221.93	363.98	90.98	130.95	7.21	173.04	2.69

The lowest temperature difference is 25% engine load at 20 MPH which produces a total power output of 78.24 Watts. The greatest temperature difference is 130.95°C at 100% engine load and 80 MPH which produces a total of 173.04 Watts.

From the results, it can be concluded that in the cold January winter, the TEGs expect to experience the greatest temperature difference, thus, the greatest total power output which ranges from 104.4 Watts to 220.08 Watts. During the hot summer in July, the TEGs are expected to experience the smallest temperature differences. The total power output ranges from 78.24 Watts to 173.04 Watts in July. The standard ambient temperature of 20°C falls between the January and July conditions by having a total power output ranging from 87.36 Watts to 186.96 Watts.

8.0 Cost Analysis

8.1 Bill of Materials

Table 20 summarizes the cost of our device mounted between an existing exhaust stack and heat shield. The weight of each part was calculated by multiplying the volume provided by the SOLIDWORKS model, and the density of each material. The cost of aluminized steel type 1 was determined from the bulk pricing listed on dir.indiamart.com (dir.indiamart, n.d.). The cost of silicone rubber is from GRANTA. The screws, washers, and hex nuts are from McMaster-Carr. These screws are for installing the TEGs to the hexagonal wall. Four screws are needed per one TEG. The full assembly procedure can be found in Section 8.2.1. Note that taxes, shipping, labor, and manufacturing are not included in these costs.

Table 20: Bill of Materials

Materials	Quantity	Size	Cost per Unit	Total
TEGs (HZ-14HV)	24	2.44” x 2.44”	$25.00 ea.	$600.0
Screws and Washers	4 packs of 25 screws and washers	#8 x ¼” Stainless Steel	$13.70 per pack	$54.80
Hex Nuts	1 pack of 100 nuts	Steel-Class 8 M2 Thread	$1.59 per pack	$1.59
Hexagonal Wall (Aluminized Steel Type 1)	1.15 kg	Section 4.1	$1.24/kg*	$1.41
Rain Cap (Aluminized Steel Type 1)	0.84 kg	Section 4.2	$1.24/kg*	$0.96
2 Structural Supports (Aluminized Steel Type 1)	1.00 kg	Section 4.3	$1.24/kg*	$1.24
2 Silicone Buffers	0.06 kg	Section 4.4	$4.00/kg	$0.24
Total				**$660.24**

**These prices are for a bulk quantity of 2000 kg minimum order.*

8.2 Manufacturing

The prices listed in the bill of materials are only estimates of material cost, and the additional cost for tooling and labor was not a factor in the bill of materials. The support structures for the hexagonal wall are the most intricate part of the assembly and would require the most time to manufacture. If this device were to be produced on a larger scale, then die-cast or investment casting would be the superior method to using a CNC machine and welding the supports by hand.

8.2.1 Assembly Procedure

Assuming that the exhaust stack is already installed on the semi-truck, our device can be manufactured in separate parts and then welded together around the existing parts for assembly. The heat shield needs to be removed for this installation and replaced after the device is attached to the exhaust pipe. The hexagonal wall can be constructed in two halves from the aluminized steel sheets that would be cut and drilled via a boring machine to create the screw holes for the TEGs. The open sides of the hexagonal wall can be attached to each other via welding. The two halves of the hexagonal wall can then be welded together around the exhaust stack of the semi-truck. The support structures would be manufactured in two, and also placed around the exhaust stack to be welded together. An assembly showing the heat shield with a wireframe view of all the components for visual clarity is shown in Figure 42.

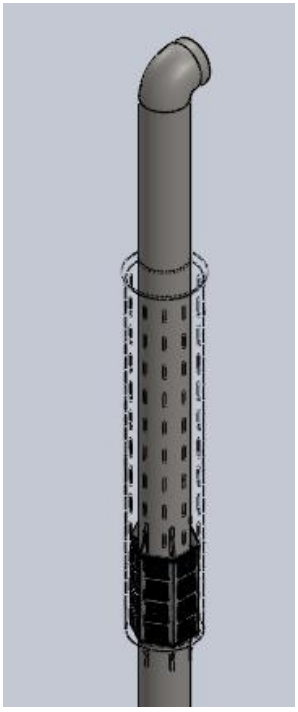

Figure 42. Wireframe Heat Shield View of Exhaust Stack and Heat Shield Assembly

8.3 Savings

The fuel cost savings can be calculated using Equation 17 which is based on the efficiencies of the different components in the system (Jaziri, et al., 2020). The efficiency of the thermoelectric generator (η_{TEG}) is listed in Section 7.3 in Tables 8-19. The alternator's efficiency

(η_{ALT}) is approximately 60% and the exhaust gases (η_{EG}) efficiency is approximately 40% (Jaziri, et al., 2020). The engines thermal efficiency (η_{ENG}) is based on the engine load conditions shown in Table 21 (Nesrine, J., et al, 2020).

$$\text{Fuel Cost Savings} = \frac{\eta_{TEG} \times \eta_{EG}}{\eta_{ALT} \times \eta_{ENG}} \times Fuel\ Cost \qquad \text{[Eq. 17]}$$

Table 21: Engine Efficiency (Wang et al., 2014)

Engine Load	25%	50%	75%	100%
Engine Efficiency	38.11%	41.72%	42.15%	41.81%

The cost analysis was calculated using the average cost of diesel fuel across the United States in 2019, which was $3.06 (U.S. EIA, 2020). Class 8 heavy duty trucks or semi-trailer trucks drive on average 62,751 miles in a year and typically get 5.8 miles per gallon (Shea, 2014; U.S. Department of Energy, 2020). The fuel savings from our device was calculated based on the minimum TEG efficiencies from operating at 25% engine load with a vehicle speed of 20 MPH. The smallest resulting efficiency is considered because the savings is expected to be greater and the payback period is expected to be shorter than the calculated result. For ambient temperatures of 20℃, the efficiency of the TEGs is 1.99%. Based on these values, the fuel cost savings was calculated as follows:

$$\left[\frac{(0.0199 \cdot 0.4)}{(0.4 \cdot 0.3811)}\right] \cdot \$3.06 \ = \ \$0.1598\ savings\ per\ gallon$$

$$(10819.1\ gallons/year)(\$0.1598\ savings\ per\ gallon) \ = \ \$1728.89\ savings/year$$

At a constant ambient temperature of 20℃, the fuel savings is $1728.89 per year. To calculate the time it would take to pay back the cost of our device, Equation 18 was used. The payback period was calculated against the material costs of our device listed in Section 8.1. Labor and manufacturing costs would increase this value.

$$\frac{Cost\ Of\ Materials}{Savings/Year} = \#\ of\ Years \qquad \text{[Eq. 18]}$$

$$\frac{\$660.24\ cost\ of\ materials}{\$1728.89\ savings/year} = 0.3819\ years$$

$$0.3819\ years \times 365\ days\ =\ 140\ days$$

The maximum payback period for the cost of our device is about 140 days. Due to the fact that this payback period was calculated with the smallest TEG efficiency, it is realistically expected that the payback period would actually be shorter than 140 days.

For January, at 25% engine load and a vehicle speed of 20 MPH, the efficiency of the TEG modules is 2.27%. Using Equations 17 and 18 again, the savings and payback time for January conditions is calculated as:

$$[\frac{(0.0227 \cdot 0.4)}{(0.4 \cdot 0.3811)}] \cdot \$3.06\ =\ \$0.1823\ savings\ per\ gallon$$

$$(10819.1\ gallons/year)(\$0.1823\ savings\ per\ gallon)\ =\ \$1972.32\ savings/year$$

$$\frac{\$660.24\ cost\ of\ materials}{\$1972.32\ savings/year} = 0.3348\ years$$

$$0.3348\ years \times 365\ days\ =\ 122.2\ days$$

If this device operated in January conditions continuously for a year, the expected fuel savings is $1972.32 and the payback time is about 123 days. For July conditions which realistically has the actual minimum TEG efficiency expected because the temperature difference is the smallest, the fuel savings is calculated as follows:

$$[\frac{(0.0189 \cdot 0.4)}{(0.4 \cdot 0.3811)}] \cdot \$3.06\ =\ \$0.1518\ savings\ per\ gallon$$

$$(10819.1\ gallons/year)(\$0.1518\ savings\ per\ gallon)\ =\ \$1642.34\ savings/year$$

$$\frac{\$660.24\ cost\ of\ materials}{\$1642.34\ savings/year} = 0.402\ years$$

$$0.402\ years \times 365\ days\ =\ 147\ days$$

The maximum payback period expected is 147 days if the device continuously operated in July conditions and if the semi-truck had a constant speed of 20 MPH.

9.0 Discussion

The results of this project had met most expectations, but had fallen short on others. For one, it was expected that the TEGs on our device would reach efficiencies of at least 5% like most modern TEGs, but the maximum efficiency from all our simulation results was 3.18% (Enescu, 2018). It was also assumed that TEGs would produce a power output between 1 and 125 Watts (Enescu, 2018). The power output results for one TEG from all our simulations ranges between 3.26 Watts and 9.17 Watts (Section 7.3).

Despite the low efficiencies and power output of the thermoelectric generators that were acknowledged at the beginning of this project, the fuel cost savings exceeded our expectations and proved the feasibility of this technology as a potential solution to recovering waste heat. When determining the feasibility of our device, the cost of materials would be $660.24 and the minimum savings expected in one year is $1642.34 (based on July conditions). Equation 19 was used to calculate the improved fuel efficiency which is 4.96%.

$$\left[\frac{(0.0189 \cdot 0.4)}{(0.4 \cdot 0.3811)}\right] \times 100 = 4.96\% \text{ [Eq. 19]}$$

The maximum payback period of just the material costs would be 147 days (Section 8.3). The actual payback period is longer because of manufacturing and labor costs. Ultimately, the project was a success in completing theoretical work to design an original solution. Some limitations of the design may include its projected lifespan due to the absence of creep, fatigue, and vibration analyses. Hot spots should also be investigated with more detailed heat transfer analyses. A physical prototype would be able to determine these limitations.

9.1 Lifespan and Maintenance

In our simulation, at 100% engine load for July (the month with the hottest conditions), the expected TEG hot side temperature is about 221.93℃, which is still below the maximum life expectancy temperature (250℃) of the HZ-14HV modules. This proves that our device would be able to perform safely under all of the operating conditions tested. Hi-Z Technology lists the life expectancy of their TEG modules to be ten years (Hi-Technology, 2020).

Although the rain cap will reduce the device's exposure to precipitation, it is assumed that there is still potential for exposure to rain, thus, rusting is considered a possibility. The thermoelectric generators themselves are not expected to be at risk of rusting because bismuth

telluride is rated highly against corrosiveness (Keshavarz et al., 2018). The screws selected to attach TEGs to the wall face are all zinc plated to provide corrosion resistance in wet environments (McMaster, 2021). For the aluminized steel components of our module, we predict the life expectancy to be anywhere from five to ten years. Aluminized steel (type 1) also has superior performance for corrosion resistance, however, it could still rust from the inside out (AK Steel, 2018). The aluminized coating on the steel would protect the steel from rusting, but only if it is prevented from getting any scratches or cracks. Joints that are welded would be susceptible to rust, which is why the heat shield is key in protecting the components from any exposure to the elements. A common problem in exhaust systems is rusting due to moisture buildup. The colder the exhaust pipe is, the less moisture is evaporated. It is healthy for the aluminized steel to experience high temperatures for extended periods of time to allow for the evaporation of any and all moisture in the system, thus, preventing rust buildup over time ("Exhaust material - aluminized steel", 2019).

9.2 Estimation for Error

It is important to note the limitations of our analysis that may require further exploration to more accurately assess the lifetime of the device and how much power it produces. The temperature power and efficiency results are based on the graphs provided by Hi-Z Technology (Figures 3-4). The equations for the graphs from Hi-Z Technology were not provided to achieve a result more accurate than the human eye reading the figures. The data graphs were uploaded to graphreader.com to determine the exact data points. From the temperature difference data, the cold side temperatures were rounded to the nearest whole number. That cold temperature was then linearly interpolated with the temperature difference to determine the power output and the efficiency of one TEG module. The total power output of our device was calculated by multiplying the power output per one TEG by the total 24 TEGs. Although it was not possible for us to get exact data points from the graphs, our numbers are as accurate as possible. There is a level of uncertainty to these numbers, but the accuracy is adequate for our purposes.

The main limitations regarding the economics of our system is the pricing of the aluminized steel. It was difficult finding a manufacturer that would provide a quote on such a small quantity of aluminized steel needed to construct a few prototypes of our assembly. This led us to use a bulk price for aluminized steel sheets as seen in the bill of materials.

9.3 Vibration, Creep, and Fatigue

Vibrations in mechanical systems cause damage and lead to failure over time. It is best to limit how much a system vibrates to elongate the life of the part. The main contributors of vibration fatigue on our device are vibrations on the exhaust system due to the engine motor mount being worn, loose, or broken, and inconsistency in road smoothness i.e. pot holes and dirt roads. A more in-depth vibrations analysis would be necessary to accurately assess the effects natural vibrations would have on this device and its ability to withstand them. Results from this analysis would allow for better prediction of the average lifetime of the device without encountering failure.

For the materials considered in this design, the effects of creep deformation can become noticeable when a metal part is operating in a temperature 35% of the melting point for that material. It should be noted that under the most extreme temperature conditions that can be expected, this device could experience 221.93℃. The melting point of ASTM A463 aluminized steel is 1,465℃ which indicates the point of creep is 512.75℃. The device is made of aluminized steel type 1, the same material of the exhaust stack which suggests that it should be able to withstand any heat given off by the exhaust gases.

9.4 Future Development

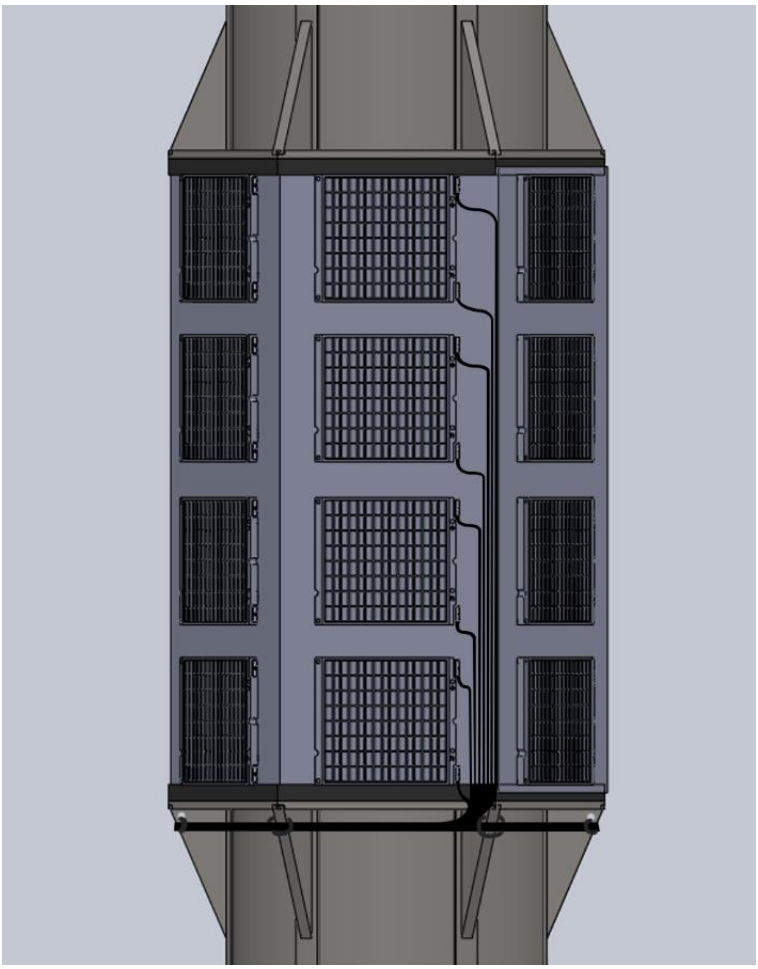

Figure 43. Schematic for Potential Wiring Configuration

A significant part of the assembly for this module would be the wiring configuration to feed into the alternator of the semi-truck. Figure 43 is a possible schematic for how the wiring could be routed. Each TEG has a positive and negative terminal. This wiring would need to be protected in some kind of thermal wrapping, and could even be all junctioned into a loom tubing that wraps around the pipe and out to the power supply. Also, constructing the system and performing testing would be another idea on how to continue this project in the future.

10.0 Conclusion

The goal of this Major Qualifying Project was to determine whether energy collection from waste heat can be implemented efficiently in an exhaust system specific to semi-trucks. With the results of this examination, it is predicted that this system would amount to a minimum fuel savings of $1642.34 per year if the device operated continuously in July conditions in Massachusetts. In regards to economic feasibility, a complete cost analysis that includes material, labor, and manufacturing costs is required. Thermoelectric power generation technology currently has a very low efficiency, but the fuel savings performance of this device model is promising for the use of TEGs in various automotive applications.

There is still some uncertainty in this device that is worth noting as well as features that could be further optimized and developed. A physical prototype was not built and tested in an environment that simulates the real-life scenario of being attached to a semi-truck. If a team or individual were to continue with this project, the next steps would be to build a working system for live testing and determine the most effective wiring configuration of the TEGs to the alternator. Additionally, these prototype tests will help guide more accurate models that take into account factors such as the flow conditions and heat transfer in the annulus of the device. Although the goals of the project were met, more work is needed to see this project in practice.

References

AK Steel. (2018). Aluminized type 1 steel. Retrieved from https://www.aksteel.com/sites/default/files/2018-02/aluminizedt1201802.pdf

AK Steel. (2018). Automotive exhaust: system materials comparator. Retrieved from https://www.aksteel.com/sites/default/files/2018-12/automotive-exhaust-comparator.pdf

Barik, R. C., Wharton, J. A., Wood, R. J. K., Stokes, K. R., & Jones, R. L. (2005). Corrosion, erosion and erosion–corrosion performance of plasma electrolytic oxidation (PEO) deposited Al2O3 coatings. Surface and coatings technology, 199(2-3), 158-167.

Bergman, T. L., Lavine, A. S., Incropera, F. P., & Dewitt, D. P. (2011). *Fundamentals of heat and mass transfer* (7th edition). John Wiley and Sons.

Chapter 2 Thermoelectric Generators (n.d.) Retrieved from http://homepages.wmich.edu/~leehs/ME539/Chapter%202.pdf

Chen, W. H., Wu, P. H., Wang, X. D., & Lin, Y. L. (2016). Power output and efficiency of a thermoelectric generator under temperature control. *Energy Conversion and Management.* Vol. 127, pp. 404-415. https://doi.org/10.1016/j.enconman.2016.09.039

Nolan, D. P. (2017). Chapter Twelve - Classified Area Pump Installations. In Fire Pump Arrangements at Industrial Facilities (Third Edition, pp. 161–167). Elsevier Inc. https://doi.org/10.1016/B978-0-12-813043-8.00012-9

Dufo-López, R., Champier, D., Gibout, S., Lujano-Rojas, J., & Domínguez-Navarroa, J. A. (2019). Optimisation of off-grid hybrid renewable systems with thermoelectric generator. *Energy Conversion and Management.* Vol. 196, pp. 1051-1067. https://doi.org/10.1016/j.enconman.2019.06.057

Enescu, D. (2018). Thermoelectric Energy Harvesting: Basic Principles and Applications. *Green Energy Advances*. https://doi.org/10.5772/intechopen.83495

Engineering ToolBox. (2003). Roughness & Surface Coefficients. Retrieved from https://www.engineeringtoolbox.com/surface-roughness-ventilation-ducts-d_209.html

Exhaust material - aluminized steel. (2019, March 06). Retrieved March 25, 2021, from https://help.summitracing.com/app/answers/detail/a_id/4778/~/exhaust-material---aluminized-steel#:~:text=If%20you%20only%20take%20short,last%208%20years%20or%20more.

Harvey, P. D. (1982). Engineering properties of steels. American Society for Metals.

Hi-Z Technology. (2020). Thermoelectric Generator Products. Retrieved from https://hi-z.com/products/

Hot dipped aluminized mild steel type 1 coil. (n.d.). Retrieved March 20, 2021, from https://www.indiamart.com/proddetail/hot-dipped-aluminized-mild-steel-type-1-coil-3789933791.html

Inventory of U.S. greenhouse gas emissions and sinks / United States (2018). Environmental Protection Agency, Office of Policy, Planning and Evaluation. U.S. Environmental Protection Agency.

Iowa80.com. (2020). Retrieved from https://www.iowa80.com/exhaust/grab-handles-guards/dynaflex-products

Keenan, J, Chao, J., & Kaye, J. (1984). Thermophysical properties of matter. (Vol. 3)

Kim, S., Park, S., Kim, S., & Rhi, S. H. (2011). A thermoelectric generator using engine coolant for light-duty internal combustion Engine-Powered Vehicles

Jääskeläinen, H. (2011, March). Exhaust System Materials. Retrieved January 03, 2021, from https://dieselnet.com/tech/diesel_exh_mat.php

Jaziri, N., Ayda, B., Jens, M., Brahim, M., Fares, T., & Ismail, M. (2020). A comprehensive review of Thermoelectric Generators: Technologies and common applications. Energy Reports. (Vol. 6) pp. 264-287. https://doi.org/10.1016/j.egyr.2019.12.011

Journal of Electronic Materials. Vol. 40, No. 5, pp. 812-816. DOI: 10.1007/s11664-011-1580-6

Kim, T., Negash, Assmelash A., & Cho, G. (2016) Waste heat recovery of a diesel engine using a thermoelectric generator equipped with customized thermoelectric modules. *Energy Conversion and Management.* (Vol. 124) pp. 280-286. https://doi.org/10.1016/j.enconman.2016.07.013

Keshavarz, M. K., Fattah-Alhosseini, A. (2018). Effect of Immersion Time on Corrosion Behavior of Single-Phase Alloy and Nanocomposite Bismuth Telluride-Based Thermoelectrics in NaCl Solution. *J. of Materi Eng and Perform* (Vol. 27) pp. 3386–3393. https://doi.org/10.1007/s11665-018-3442-3

Mamur, H. (2019). A detailed modeling of a thermoelectric generator for maximum power point tracking. *Turkish Journal of Electrical Engineering & Computer Sciences*. Vol 28, pp. 124-139. https://doi.org/10.3906/elk-1907-166

Mathers, J., Wolfe, C., Norsworthy, M., & Craft, E. (2014). The green freight handbook. *Environmental Defense Fund*.

Metric Steel Pan Head Screws with Internal-Tooth Lock Washer. (2021). Retrieved from https://www.mcmaster.com/screws/system-of-measurement~metric/thread-size~m2/length~10-mm/vibration-resistant-rounded-head-screws/

Power Generation. (2016, December 08). Retrieved January 03, 2021, from https://thermal.ferrotec.com/technology/thermoelectric-reference-guide/thermalref13/

Shea, S. (2014). Supertruck making leaps in fuel efficiency. Retrieved from https://www.energy.gov/eere/articles/supertruck-making-leaps-fuel-efficiency#:~:text=Since%202010%2C%20the%20truck%20has,5.8%20miles%20to%20the%20gallon.

Silicone Vinyl Methyl Silicone (VMQ) O-Rings & Silicone Gaskets. Seal & Design, Inc. (2021, March 15). Retrieved from https://www.sealanddesign.com/products/elastomeric-compounds/silicone-vmq/.

Saqr, K. M., & Musa, M. N. (2009). Critical review of thermoelectrics in modern power generation applications. Thermal science. Vol. 13. No. 3. pp. 165-175. DOI: 10.2298/TSCI0903165S

Steel Hex Nut. (2021). Retrieved from https://www.mcmaster.com/90592A075/

Suppes, G. J., & Storvick, T. S. (2016). Chapter 5 - The New Electric Vehicle Society. Sustainable power technologies and infrastructure: Energy sustainability and prosperity in a time of climate change. pp. 161-190. Elsevier. https://doi.org/10.1016/B978-0-12-803909-0.00005-1

Thermoelectric Properties of Materials. (n.d.). Retrieved January 03, 2021, from http://thermoelectrics.matsci.northwestern.edu/thermoelectrics/index.html

TruckPipesUSA.com. (2020). Retrieved from https://www.truckpipesusa.com/products/6-x-120-16ga-straight-aluminized-exhaust-tubing-id-od-s6-120exa.html

U.S. Department of Energy. (2020). Maps and Data - Average Annual Vehicle Miles Traveled by Major Vehicle Category. Retrieved from https://afdc.energy.gov/data/

U.S. Energy Information Administration. (2020). Weekly Retail Gasoline and Diesel Prices. Retrieved from https://www.eia.gov/dnav/pet/pet_pri_gnd_a_epd2d_pte_dpgal_a.htm

Wang, T., Zhang, Y., Zhang, J., Peng, Z., Shu, G. (2014). Comparisons of system benefits and thermo-economics for exhaust energy recovery applied on a heavy-duty diesel engine and a light-duty vehicle gasoline engine. *Energy Conversion and Management.* Vol. 84, pp. 97-107. https://doi.org/10.1016/j.enconman.2014.04.022

Washing Cars in Winter: How to Stop Rust on Cars. Windshield Repair & Replacement. (2017, February 19). https://www.safelite.com/resource-center/auto-experts/auto-experts/2017/02/19/keep-car-clean-winter#:~:text=Rust%20can%20be%20a%20serious,rigidity%20of%20the%20vehicle's%20frame.

Weather-us.com (2021). Retrieved from https://www.weather-us.com/en/massachusetts-usa-climate#climate_text_5

Weng, C., & Huang, M. (2013). A simulation study of automotive waste heat recovery using a thermoelectric power generator. *International Journal of Thermal Sciences.* Vol. 71, pp. 302-309. https://doi.org/10.1016/j.ijthermalsci.2013.04.008

White, W. (2018). Advanced Highway Maintenance and Construction Technology (AHMCT) Research Center. *Natural Frequencies of Pickups and Medium and Heavy Trucks for Use in Component Design.* https://dot.ca.gov/-/media/dot-media/programs/research-innovation-system-information/documents/preliminary-investigations/truck-natural-frequency-pi-a11y.pdf

Witting, I. T., Chasapis, T., C., Ricci, F., Peters, M., Heinz, N. A., Hautier, G., & Snyder, J. S. (2019). The Thermoelectric Properties of Bismuth Telluride. *Advanced Electronic Materials*. Vol. 5. No. 6. https://doi.org/10.1002/aelm.201800904

Yang, G., Xu, H., Wang, Z., & Tian, Z. (2016). Truck acceleration behavior study and acceleration lane length recommendations for metered on-ramps. International Journal of Transportation Science and Technology, 5(2), 93–102. https://doi.org/10.1016/j.ijtst.2016.09.006

Appendices

Appendix A: Stress and Strain Theoretical Calculations

The gravitational force:

$$F_g = mg = (m_{wall} + m_{TEGs})g = (1.147\ kg + 1.56\ kg)(9.81\ m/s^2) = 26.5\ N$$

The force in the y-direction:

$$F_y = F_g + F_c$$

$$F_y = (26.5\ N) + (10\ N) = 36.5\ \text{N}$$

The stress and strain was calculated as follows:

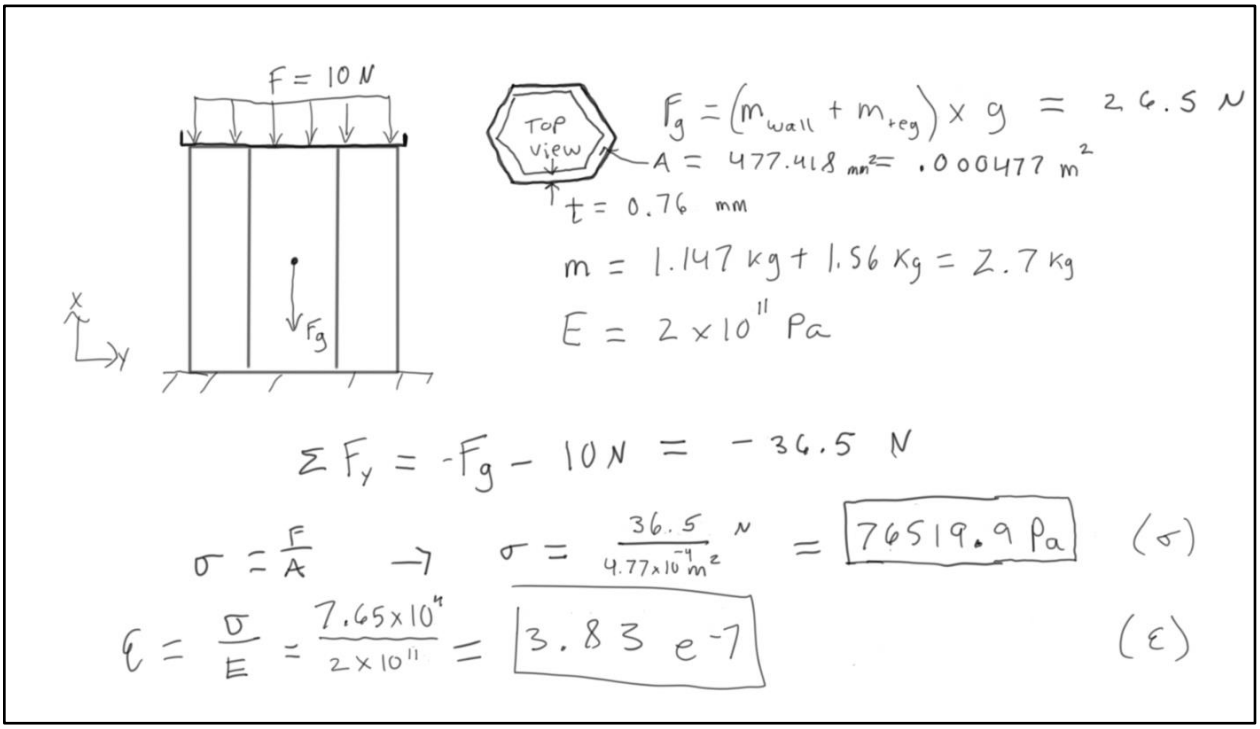

Figure A1. Written Calculated Stress and Strain on the Hexagonal Wall

The vertical stress and strain of the hexagonal wall was obtained by assuming a compression force from the fixturing to the pipe of about 10 N. This force is added to the force of gravity applied on the wall and were able to obtain a value for estimated stress. From here, Hooke's Law was used to determine the strain on the wall with the following relationship:

$$\varepsilon = \frac{\sigma}{E}$$

Appendix B: Material Properties used in SOLIDWORKS and Ansys Structural Analysis

Property	Value	Units
Elastic Modulus	2e+11	N/m^2
Poisson's Ratio	0.29	N/A
Shear Modulus	7.5e+10	N/m^2
Mass Density	7870	kg/m^3
Tensile Strength	310000000.6	N/m^2
Compressive Strength		N/m^2
Yield Strength	166000000.8	N/m^2

Figure B1. Material Properties of Aluminized Type 1 Steel

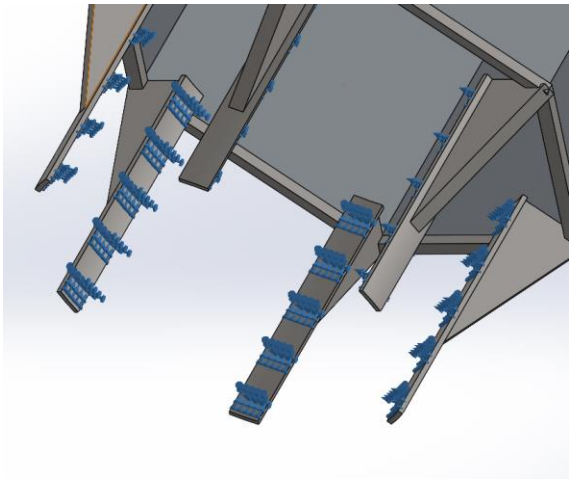

Figure B2. Defined Fixed Supports

.

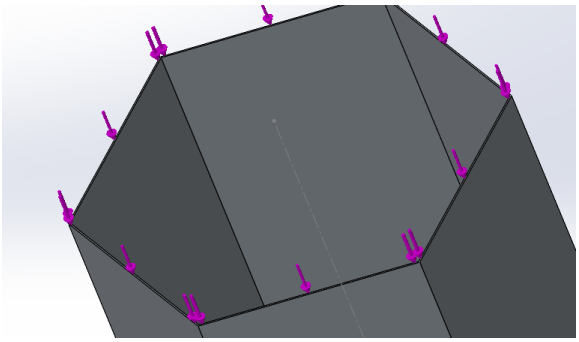

Figure B3. Surface of Force Applied in the SOLIDWORKS Simulation

Appendix C: Thermal Analysis Theoretical Calculations

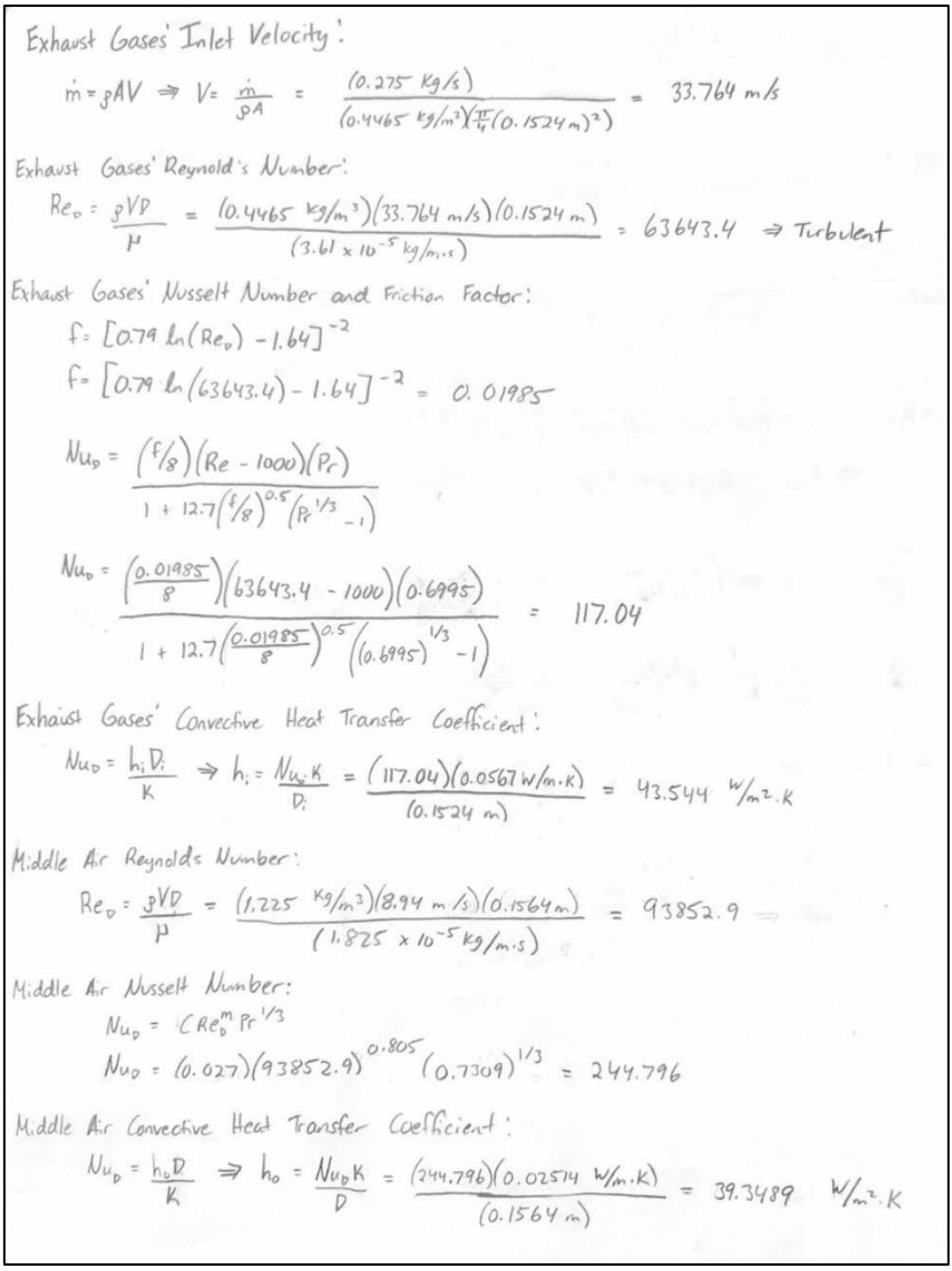

Figure C1. Written Thermal Theoretical Calculations Part One

$$R_{tot} = \frac{1}{h_i \pi D_i L} + \frac{\ln(D_o/D_i)}{2\pi K_1 L} + \frac{1}{h_o \pi D_o L}$$

$$\frac{1}{h_i \pi D_i L} = \frac{1}{(43.544\ W/m^2 \cdot K)\pi(0.1524 m)(2.54 m)} = 0.018884\ K/W$$

$$\frac{\ln(D_o/D_i)}{2\pi K L} = \frac{\ln(0.1564 m / 0.1524 m)}{2\pi(42\ W/m \cdot K)(2.54 m)} = 3.8652 \times 10^{-5}\ K/W$$

$$\frac{1}{h_o \pi D_o L} = \frac{1}{(39.3489\ W/m^2 \cdot K)\pi(0.1564 m)(1.2192 m)} = 0.042423\ K/W$$

$$\Rightarrow R_{tot} = 0.061346\ K/W$$

$$\frac{T_\infty - T_{out}}{T_\infty - T_{in}} = \exp\left(\frac{-1}{\dot{m} C_p R_{tot}}\right)$$

$$\Rightarrow \frac{293 K - T_{out}}{293 K - 792 K} = \exp\left(\frac{-1}{(0.275\ kg/s)(1097.18\ J/kg \cdot K)(0.061346 K/W)}\right)$$

$\Rightarrow$ Exhaust Pipe Outlet Temperature: $T_{out} = 765.756 K$

Average Exhaust Gas Temperature:

$$T_{ave} = \frac{T_{out} + T_{in}}{2} = \frac{765.756 K + 792 K}{2} = 778.878\ K$$

Figure C2. Written Thermal Theoretical Calculations Part Two

Appendix D: Ansys Thermal Analysis 3D Simulation Setup

The 3D model's named selections of the inlets and outlets were as follows:

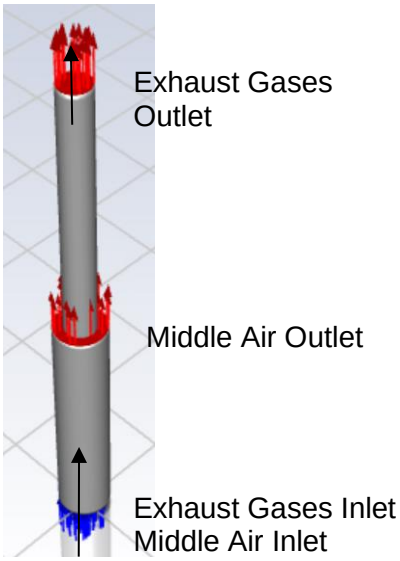

Figure D1. 3D Simulation Inlet/Outlet Named Selections

Energy was turned on to model heat transfer from the exhaust gases and turbulent flow settings were used. To simulate turbulent exhaust gas flow, under "General" conditions and "Viscous Model", the model was set to "k-epsilon (2 eqn)," K-epsilon Model set to "Realizable," and Near-Wall Treatment was set to "Enhanced Wall Treatment" as seen in Figure D2. All other options under Viscous Model were left as the default.

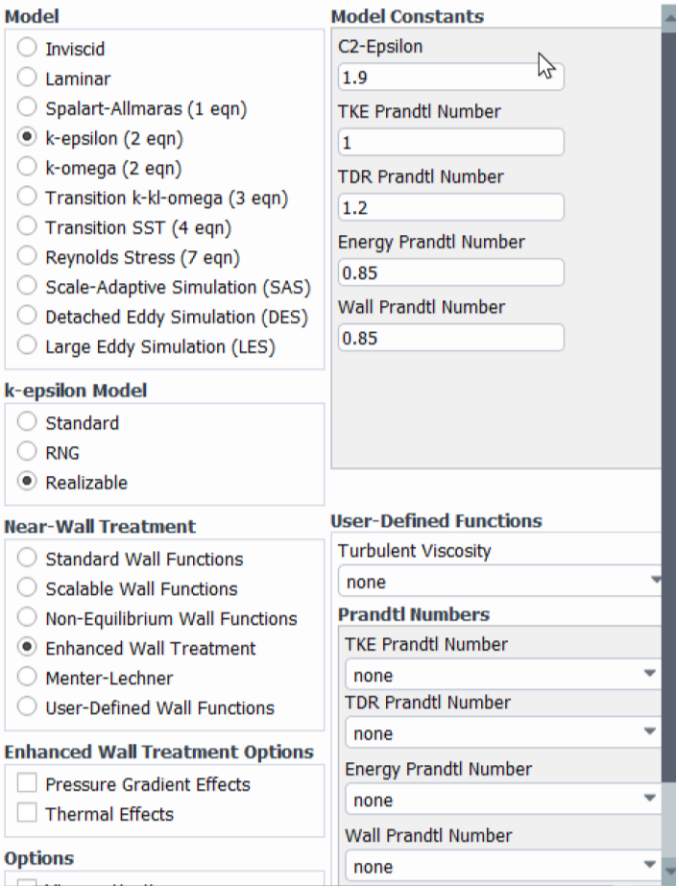

Figure D2. Viscous Model Settings

Figure D3 shows the listed boundary condition names of all the inlets, interiors, and outlets.

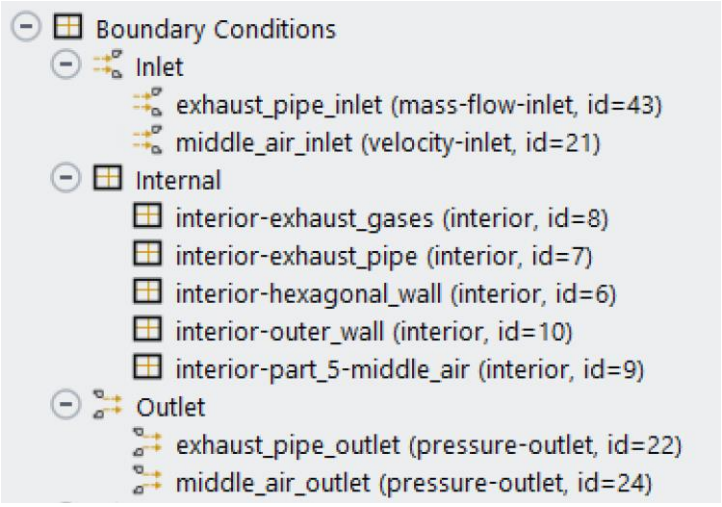

Figure D3. Inlet, Internal, and Outlet Boundary Conditions

Table D1 shows the inlet and outlet conditions of the model used for an ambient temperature of 20℃ or 293K. In the January and July simulations, the 293 K boundary condition was changed to -6.95°C and 32.2°C, respectively.

Table D1. Ansys Inlet and Outlet Conditions

Name	Type	Conditions	Value
Exhaust Pipe Inlet	Mass Flow Inlet	Mass Flow Rate	See Table 6
		Thermal Total Temperature	See Table 6
Middle Air Inlet	Velocity Inlet	Velocity Magnitude	0 m/s
		Thermal Temperature	293 K
Exhaust Pipe Outlet	Pressure Outlet	Gauge Pressure	0 Pascals
		Backflow Total Temperature	293 K
Middle Air Outlet	Pressure Outlet	Gauge Pressure	0 Pascals
		Backflow Total Temperature	293 K

Figure D4 shows the named selections of the wall parts to the system. In 3D models, Ansys automatically creates a wall "shadow" which considers both sides of the wall. All of the walls are set at "Via System Coupling."

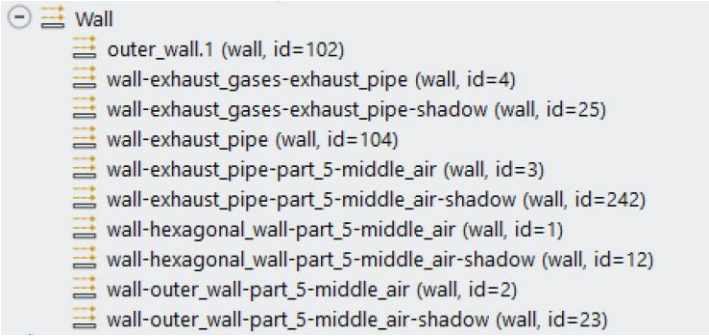

Figure D4. Named Variable Selections of Walls

The simulation used hybrid initialization and 200 iterations in the final calculation.

Appendix E: Ansys Thermal Analysis 2D Simulation Setup

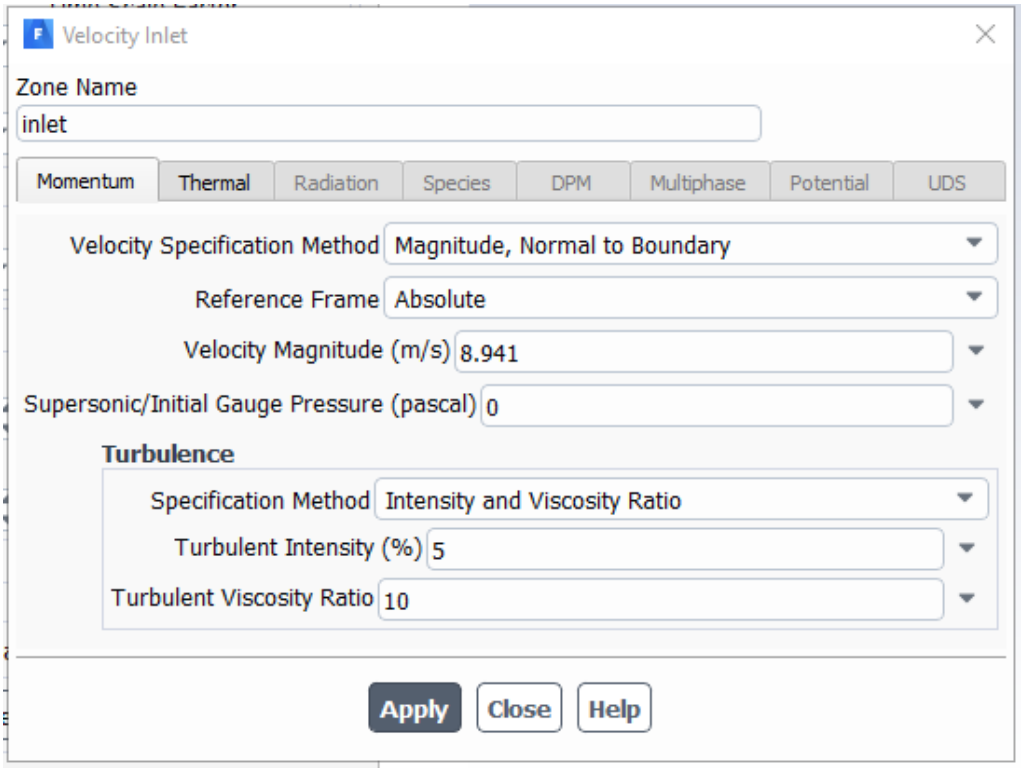

Figure E1. Inlet Velocity Boundary Condition

Figure E1 displays the inlet air velocity and direction being set for the 2D simulations.

Figure E2. Inlet Temperature Boundary Condition

The inlet air temperature being set is shown by Figure E2 for the 2D simulations.

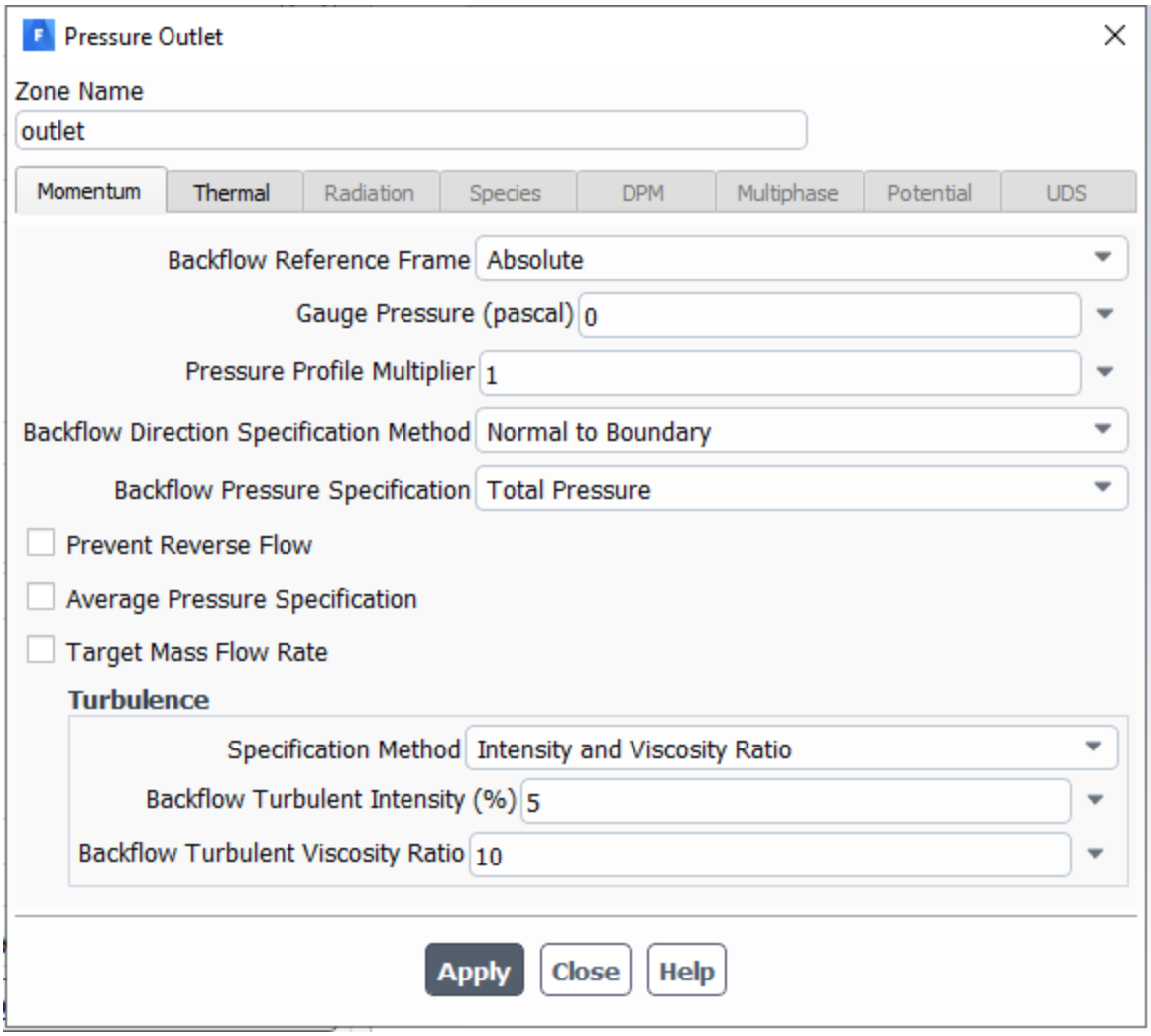

Figure E3. Outlet Pressure Boundary Condition

Outlet pressure was also set for the 2D simulations as shown by Figure E3.

Figure E4. Outlet Temperature Boundary Condition

This is the outlet air temperature being set for the 2D simulations, as shown in Figure E4.

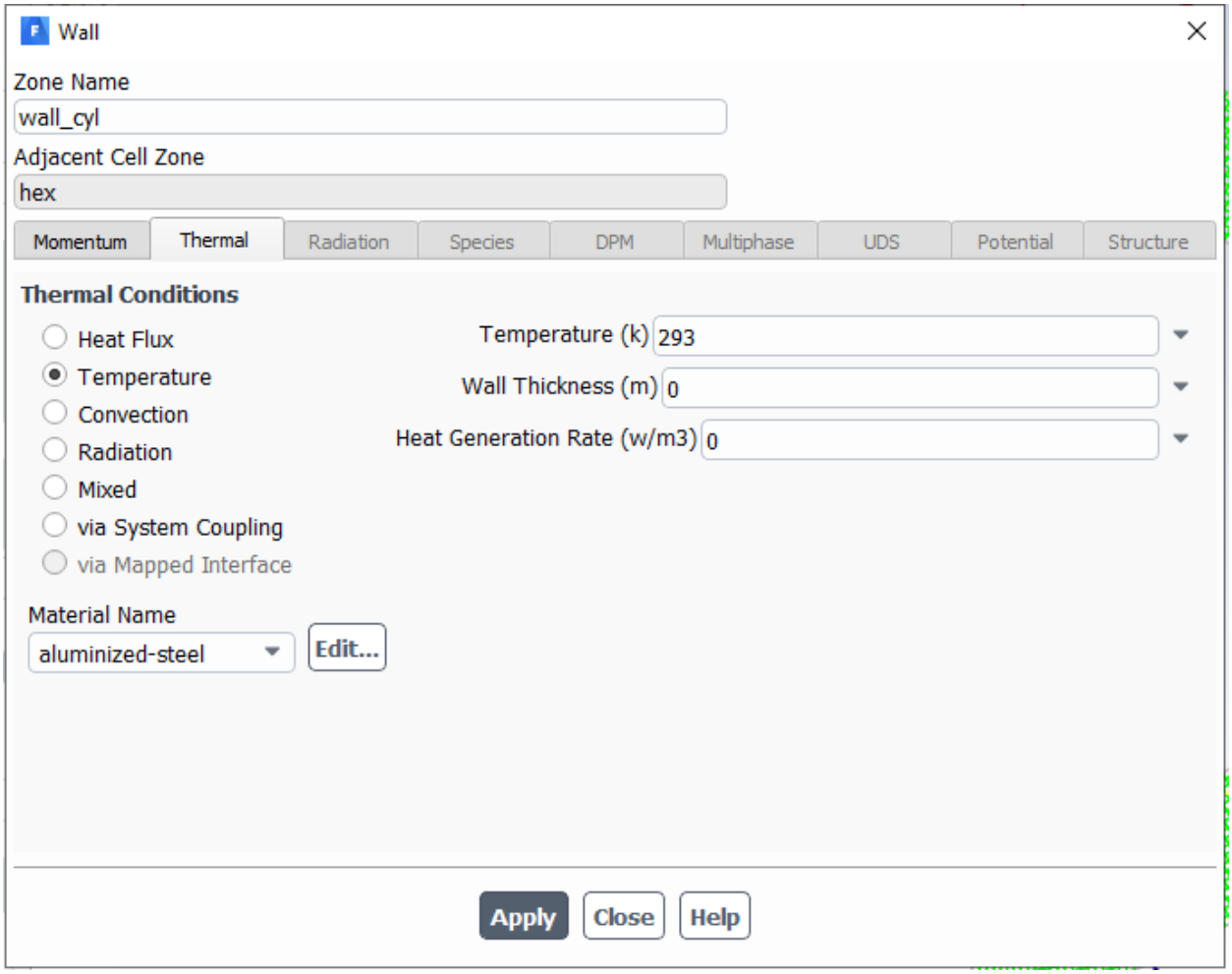

Figure E5. Heat Shield Temperature Boundary Condition

The heat shield wall temperature and material is being set in Figure E5 for the 2D simulations.

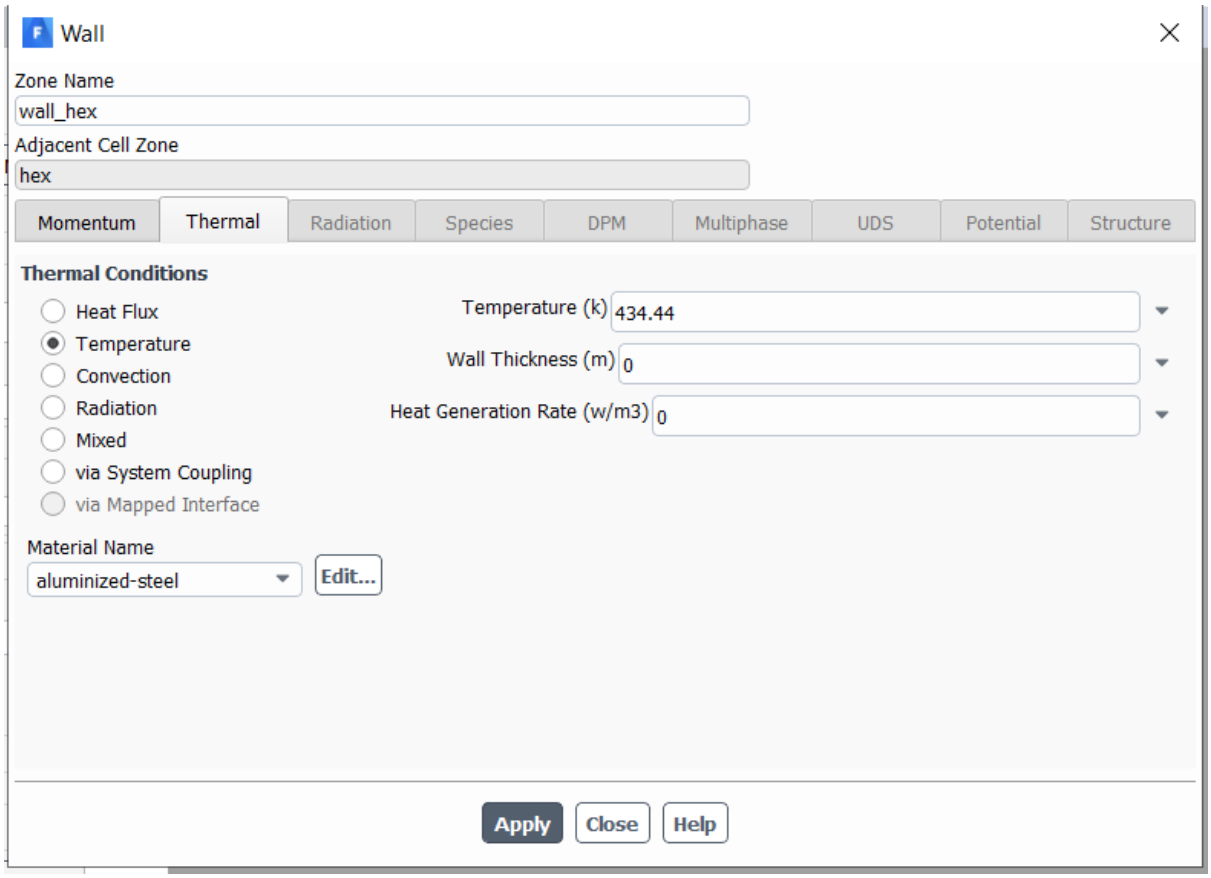

Figure E6. Hexagonal Wall Temperature Boundary Condition

The hexagonal wall temperature is being set in Figure E6.

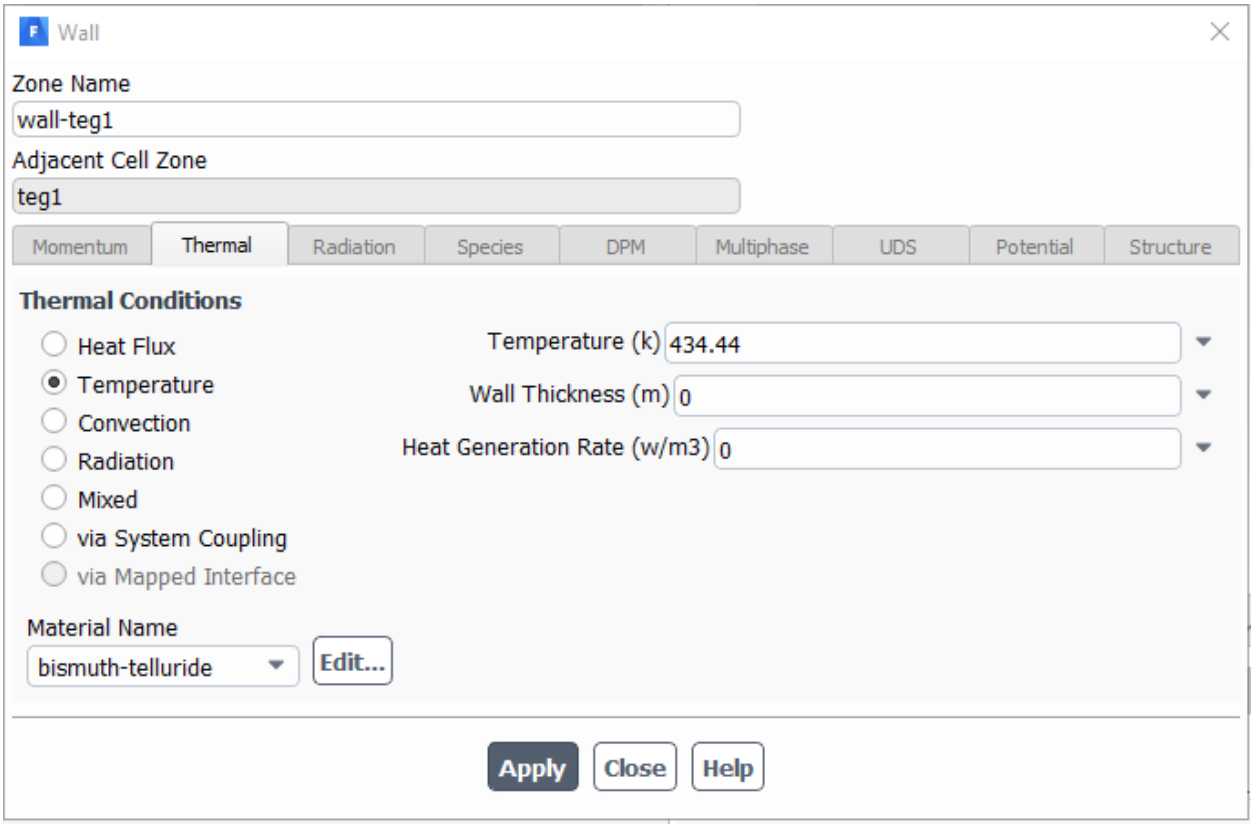

Figure E7. TEG Temperature Boundary Condition

Figure E7 displays the temperature and material being set of one out of the three TEGs for the 2D simulations.